HF SC Hydraulic Fracturing & Sand Control
JOINT INDUSTRY PROJECT
THE UNIVERSITY OF TEXAS AT AUSTIN
http://www.cpge.utexas.edu/hfsc

Report # 2015HFSC00001

A critical reexamination of methods for picking closure pressure from diagnostic fracture injection tests

Mark W. McClure[1], Hojung Jung[1], Dave D. Cramer[2], and Mukul M. Sharma[1]

[1]The University of Texas at Austin, Department of Petroleum and Geosystems Engineering

[2]ConocoPhillips

Presented at the 9th Annual Meeting of the Hydraulic Fracturing and Sand Control Joint Industry Project held at the AT&T Executive Education and Conference Center, Austin, TX, U.S.A. on April 29th – May 1st, 2015.

A critical reexamination of methods for picking closure pressure from diagnostic fracture injection tests

Submission to SPE Journal - August 2015

Resubmission of SPE 170956

Mark W. McClure[1], Hojung Jung[1], Dave D. Cramer[2], and Mukul M. Sharma[1]

[1]The University of Texas at Austin, Department of Petroleum and Geosystems Engineering

[2]ConocoPhillips

Abstract

In this study, we present a new method for interpreting diagnostic fracture injection test (DFIT) data. The method is based on results from a three-dimensional hydraulic fracturing simulator that allows fractures to retain aperture after mechanical closure. After closure, an empirical, non-linear joint closure law is used to relate fracture aperture and stiffness to the effective normal stress. Fracture closure increases fracture stiffness, which, in low permeability formations, causes an increase in the pressure derivative. The resulting pressure signal in a *G*-function analysis plot has often been incorrectly attributed to fracture height recession or closing of secondary transverse fractures, leading to a misidentification of closure pressure. Based on our simulation results, we recommend best practices for estimating closure pressure, which we validate with a series of numerical simulations and field examples.

Results from this method are compared with results from other methods that are commonly used for picking closure pressure from minifrac, extended leakoff, or diagnostic fracture injection tests. The comparisons show that common methodologies for interpreting closure pressure can lead to significant error. We recommend picking closure at the first point of deviation from linearity on a plot of pressure versus the square root of time or *G*-time (after the very early-time transient associated with wellbore and near wellbore friction and fracture tip-extension has dissipated). In low permeability formations, this interpretation can be assisted by identifying the upward deflection on a plot of $G \times dP/dG$. Other methods for identifying closure have used Bourdet plots with either: (1) pressure derivative taken with respect to superposition time or (2) time-integrated pressure. Our results show that these methods often yield unreliable or ambiguous interpretations.

First, we show series of generic numerical simulations to demonstrate the effect of key input parameters. The governing equations of a DFIT pressure transient are derived and used to demonstrate the importance of changing fracture aperture after closure on the pressure transient behavior. Next, three field examples of DFITs are provided with simulations that closely match the data. The simulation matches provide assessments of the minimum principal stress, which are then compared to estimates from different graphical techniques for picking closure. Third, a field example is presented in which downhole tiltmeter measurements provide an independent estimate of the minimum principal stress. Finally, we provide discussion of non-uniqueness and the opportunity to further validate our method using pump-in/flow-back tests.

1. Introduction

1.1 Background

Diagnostic fracture injection tests (DFIT) are used for a variety of purposes, including measuring the magnitude of the minimum principal stress in a formation. Fluid, usually untreated clear water, is injected at a low to moderate rate for a short period of time, creating a relatively small hydraulic fracture, and then the well is shut in. The pressure transient following shut-in is analyzed to identify the closure pressure, defined as the fluid pressure at which the fracture walls come into contact. The closure pressure is taken to be an estimate of the minimum principal stress. In recent years, there has been a growing interest in using DFITs to evaluate very low permeability formations, including shale reservoirs. DFITs belong to a family of fracture-injection/falloff tests that includes minifrac and extended leakoff tests (XLOT). These fracturing tests have been interpreted with a variety of different methods and used for many decades (Hubbert and Willis, 1957; Godbey and Hodges, 1958; Haimson and Fairhurst, 1967). Nevertheless, there is still not universal agreement on best practices for using them to estimate the minimum principal stress.

Figure 1 shows an example of pressure data from a DFIT, with different stages of the test numbered. Injection is performed, typically at constant rate, for several minutes. Initially, pressure rises linearly with time, as relatively little fluid leaks out into the formation and the transient is dominated by wellbore storage (1). At the leakoff point (LOP), the transient deviates from linearity, indicating that a hydraulic fracture has formed at the wellbore, and has grown sufficiently large that it has a non-negligible effect on the pressure behavior. In Figure 1, a LOP is not apparent. Instead, there is a breakdown pressure when the fracture forms and causes an abrupt drop in pressure (2). As the fracture grows larger, propagation is aided by the concentration of stress at its tip, and the pressure drops down to the fracture propagation pressure (3). During propagation, injection pressure is mostly constant, but may be gradually increasing or decreasing. When injection is stopped, there is an immediate drop in pressure to the initial shut-in pressure (ISIP) as wellbore and near wellbore frictional pressure drop reduces (4). Subsequently, the pressure continues to fall off, and the fracture closure pressure (FCP) is reached when the walls of the fracture come into contact (5).

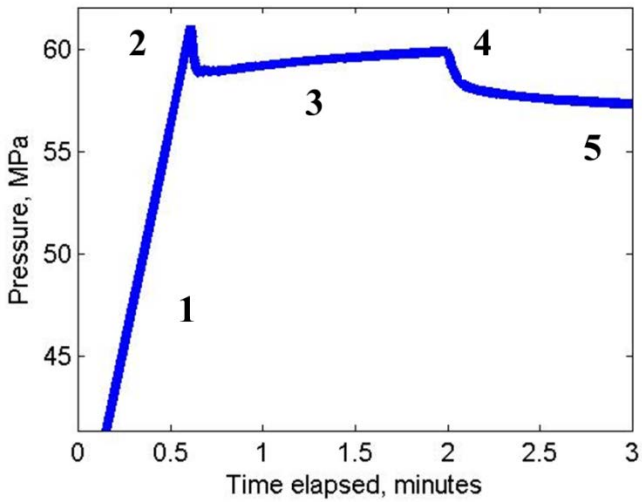

Figure 1: Schematic of a diagnostic fracture injection test. Numbered points are described in the text.

Zoback (2007) provides a detailed description of this process and the relationship between the observations and the minimum principal stress. In an ideal case, the fracture will be able to propagate with a fluid pressure only slightly greater than the minimum principal stress, and the ISIP and FCP should be very close together. However, in some cases, ISIP can be considerably higher than the FCP, which is why methods for estimating fracture closure pressure are required. The LOP may be used to estimate the minimum principal stress but is considerably less reliable.

The conventional method for interpreting the fracture closure pressure is to plot pressure versus the square root of time or a specialized function of time called the *G*-function (Nolte, 1979; Nolte and Smith, 1981). For one-dimensional leakoff of fluid from a constant pressure boundary, the solution to the diffusivity equation predicts that the leakoff rate will scale with the inverse of the square root of time. When coupled with a wellbore/fracture system of constant compliance, the result is pressure decay scaling with the square root of time (see Appendix B for a full derivation). The *G*-function is a generalization of this concept that includes the effect of fracture propagation (which causes the duration of leakoff to be different at each point along the fracture).

On either plot, pressure is expected to form a straight line prior to closure and deviate from the straight line when closure occurs. Therefore, the deviation of pressure from the straight line can be used to identify the fracture closure pressure, an estimate of the minimum principal stress (Castillo, 1987; Zoback, 2007). In addition, $G \times dP/dG$ versus G is often plotted (equivalent to $dP/d(\ln(G))$ versus G). As long as pressure forms a straight line, $G \times dP/dG$ should also form a straight line, and so closure can be picked at the deviation from the straight line (Barree and Mukherjee, 1996).

Unfortunately, plots of pressure versus *G*-time often yield curving lines with multiple points of inflection. Efforts have been made to interpret and explain these non-ideal observations. Wellbore and near wellbore pressure drop, pressure dependent leakoff, fracture height recession, closing of secondary transverse fractures, and fracture tip extension are some of the most commonly cited sources of non-ideal behavior (Nolte, 1991; Nolte et al, 1993; Barree and Mukherjee, 1996; Barree, 1998; Box 9F from Economides and Nolte, 2000; Barree et al., 2007).

Injection of proppant and complex fluids further complicates interpretation, which is why diagnostic fracture injection tests are performed with clear water.

In high permeability formations, leakoff limits fracture length and closure occurs rapidly. But in very low permeability formations, closure can occur hours or days after shut-in. In DFITs, non-ideal transients are nearly always observed. For example, Figure 2 shows an example of a DFIT test from a very low permeability shale formation. The x-axis is *G*-time, which is a non-linear function of shut-in time (Nolte, 1979; Barree et al., 2007). A *G*-time equal to zero is equivalent to the moment of shut-in.

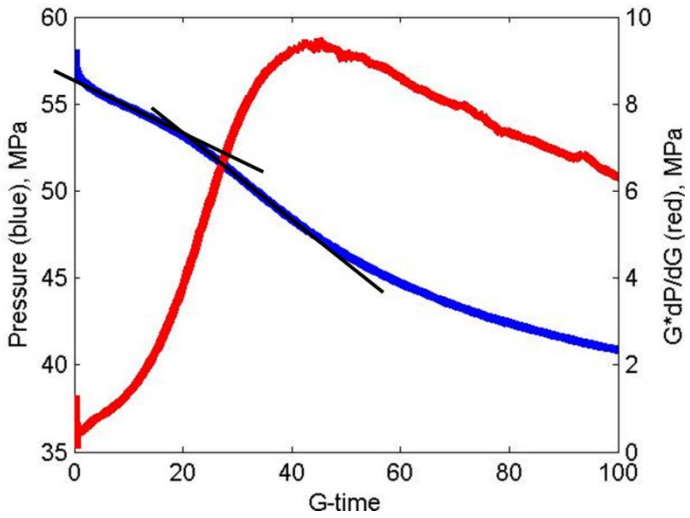

Figure 2: Field DFIT #1. Further discussion is provided in Section 3.2. This transient was originally shown in Figure 4 by Cramer and Nguyen (2013). Two different straight line trends are shown with black lines.

Figure 2 shows that pressure undergoes multiple inflection points during the shut-in period, with a very high derivative upon shut-in, then a sharp drop in derivative, a gradual increase in derivative, and finally an extended decline. It is not obvious how to pick closure by identifying the departure from linearity from the *P* versus *G* curve (Castillo, 1987; Zoback, 2007). A straight line could plausibly be identified as ending at roughly 10 *G*-time or at roughly 35 *G*-time. In this paper, we demonstrate that the closure should be picked at the end of the first linear trend (Section 3.2). Common industry methodologies would pick closure at the end of the second linear trend.

A diverse literature has evolved on DFIT interpretation, discussing topics such as interpretation of formation properties such as permeability and reservoir pressure, diagnosis of non-ideal reservoir behavior, and practical aspects of test design and implementation (Nolte, 1991; Nolte et al., 1993; Barree and Mukherjee, 1996; Barree, 1998; Craig and Blasingame, 2006; Barree et al., 2007; Marongiu-Porcu et al., 2011, 2014; Mohamed et al., 2011; Soliman and Kabir, 2012; Soliman and Gamadi, 2012; Cramer and Nguyen, 2013; Padmakar, 2013; McClure, 2014a; Wallace et al., 2014; Meng et al., 2014; Barree et al., 2014; Craig, 2014). Our focus in this paper is specifically on the estimation of the minimum principal stress from the fracture closure pressure. This paper elaborates on concepts originally introduced by McClure et al. (2014).

1.2 Methods in the literature for picking closure

A variety of guidelines for picking fracture closure pressure from DFITs have been provided in the literature. A few of these methods are summarized in this section.

1.2.1 G-function plots

Identification of fracture closure pressure and non-ideal behavior is usually done using plots of pressure and $G\times dP/dG$ versus G-time. An "ideal" DFIT has a $G\times dP/dG$ curve that is straight until closure, and then a hump before curving downward and flattening out. A concave upward $G\times dP/dG$ curve is traditionally interpreted as being caused by fracture height recession or transverse fracture storage. A concave downward $G\times dP/dG$ is interpreted as being caused by pressure dependent leakoff or fracture tip extension. These interpretations are based on numerical simulations (Nolte, 1991; Barree and Mukherjee, 1996; Barree, 1998) and are used widely across the industry (Economides and Nolte, 2000; Barree et al., 2007; Soliman and Gamadi, 2012; Soliman and Kabir, 2012; Cramer and Nguyen, 2013; Wallace et al., 2014; Meng et al., 2014; Barree et al., 2014).

When the $G\times dP/dG$ curve is concave upward, closure is traditionally picked by drawing a straight line from the origin, tangent to the $G\times dP/dG$ curve. The point of tangency is the time of closure, and the fracture closure pressure is identified as the pressure at that time. This is typically equivalent to picking closure at the end of the second straight line on a plot of pressure versus G-time, as shown from comparison of Figure 17 and Figure 2. When the $G\times dP/dG$ curve is concave down, closure is picked at around the time the $G\times dP/dG$ curve stops increasing.

1.2.2 Bourdet plots with derivative with respect to superposition time

Mohamed et al. (2011) and Marongiu-Porcu et al. (2011; 2014) advocate using Bourdet et al. (1989) plots in which the derivative is taken with respect to superposition time, rather than shut-in time. Bourdet plots are log-log plots that show the change in pressure and $dP/d(\ln(\Delta t))$ (which can be equivalently written as $\Delta t\times dP/d\Delta t$), where Δt is the time since the beginning of the transient (Bourdet et al., 1989). Figure 3 shows an example.

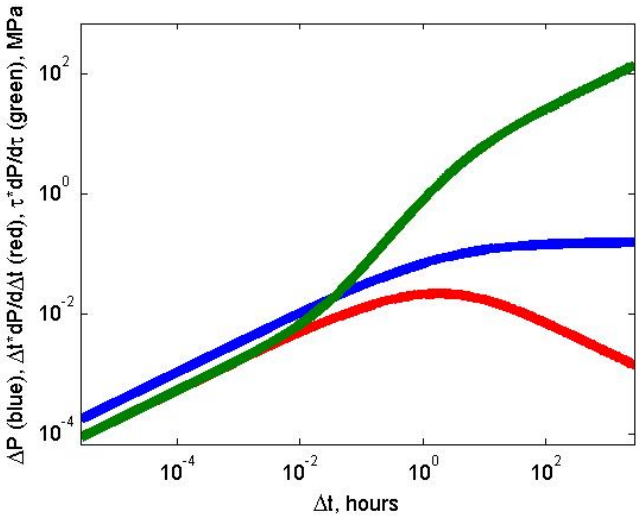

Figure 3: Generic example of a Bourdet plot with ΔP (blue) and the logarithmic derivative of ΔP taken with respect to Δt (red) and τ (green). Superposition time was calculated assuming t_e equal to 100 seconds (0.0278 hours). The green curve would have been identical if Agarwal, rather than superposition, time had been used for taking the derivative.

Superposition time can be defined a variety of ways. For the method proposed by Mohamed et al. (2011), superposition time is defined as:

$$\tau = \frac{t_e + \Delta t}{\Delta t}, \tag{1}$$

where t_e is duration of injection and Δt is the time elapsed since the end of injection. If varying flow rates are used during the injection, t_e can be calculated as the cumulative volume divided by the final injection rate (Blasingame and Lee, 1986).

The effect of taking the derivative with respect to superposition time can most easily be understood by considering the relationship with Agarwal time. Agarwal time is defined as (Agarwal, 1980):

$$t_a = \frac{t_e \Delta t}{t_e + \Delta t} = \frac{1}{\frac{1}{t_e} + \frac{1}{\Delta t}} = \frac{t_e}{\tau}. \tag{2}$$

The final equality in Equation 2 shows that, in this case, there is a simple relationship between Agarwal time and superposition time. Agarwal time is equal to one half the harmonic average of t_e and Δt. Agarwal time has the property that it is approximately equal to Δt when $\Delta t << t_e$ and approximately equal to t_e when $\Delta t >> t_e$. If Δt is much larger than t_e, taking the derivative with respect to Agarwal time is equivalent to adding 1.0 to the slope of the $dP/d(\ln(\Delta t))$ curve on the log-log plot. This is true because:

$$t_a \frac{dP}{dt_a} = t_a \frac{dP}{d\Delta t}\frac{d\Delta t}{dt_a} = t_a \frac{dP}{d\Delta t}\frac{1}{t_a^2\left(\frac{1}{t_a} - \frac{1}{t_e}\right)^2} = t_a \frac{dP}{d\Delta t}\frac{\Delta t^2}{t_a^2} = \frac{\Delta t^2}{t_a}\frac{dP}{d\Delta t} \sim \frac{\Delta t^2}{t_e}\frac{dP}{d\Delta t}, \tag{3}$$

where the final step is taken because t_a asymptotically approaches t_e for $\Delta t >> t_e$. Therefore, for $\Delta t >> t_e$:

$$\frac{d\left(\log\left(t_a \frac{dP}{dt_a}\right)\right)}{d\left(\log\left(\Delta t\right)\right)} \sim \frac{d\left(\log\left(\frac{\Delta t^2}{t_e}\frac{dP}{d\Delta t}\right)\right)}{d\left(\log\left(\Delta t\right)\right)} = \frac{d\left(\log\left(\Delta t \frac{dP}{d\Delta t}\right)\right)}{d\left(\log\left(\Delta t\right)\right)} + 1. \tag{4}$$

On a Bourdet plot, the semilog derivative curve with derivative taken with respect to Agarwal time is the same as the semilog derivative curve with derivative taken with respect to superposition time because (from Equation 2):

$$\frac{dP}{d(\ln(t_a))} = -\frac{dP}{d(\ln(\tau))}. \tag{5}$$

The change in sign does not affect the Bourdet plot because the semilog derivative is always plotted as positive on the log-log plot.

These effects can be seen in Figure 3. Initially, $\Delta t << t_e$, and so $t_a \sim \Delta t$ and all three curves have a slope of 1/2. This corresponds to the period when the curve would be linear on a plot of pressure versus the square root of time or versus G-time. As Δt gets closer to t_e, the superposition derivative curve begins to curve upward, reaching a slope of 3/2, even as the pressure and standard pressure derivative curve continue along a slope of 1/2. This transition to a 3/2 slope does not represent an actual change in the pressure transient or in the reservoir behavior. It is purely an artifact from taking the derivative with respect to superposition time (or equivalently, Agarwal time). The transition begins at about $0.1t_e$ and finishes at about $10t_e$. When the conventional derivative curve goes to a -1/2 slope, the superposition derivative line goes to a 1/2 slope.

Mohamed et al. (2011) recommend picking closure when the derivative plot changes from a 3/2 slope to a 1/2 slope. This is equivalent to a transition from a 1/2 slope to a -1/2 slope on a Bourdet derivative with respect to Δt. The -1/2 slope occurs because it is the late time "impulse" solution for linear flow. It can be shown that if a small volume of fluid is injected, and then the well is shut-in, then the late-time pressure transient can be found by taking the derivative of the analytical solution for constant rate injection under the same conditions (Houze et al., 1988). The analytical solution for the pressure change due to constant rate injection under a linear flow regime scales with the square root of time (Gringarten et al., 1974) and so the derivative of that solution, the impulse solution for linear flow, scales with the inverse of the square root of time. Thus, the method of picking closure provided by Mohamed et al. (2011) is equivalent to picking closure when the "impulse" period begins in the transient.

A straight line on a pressure versus square root of time or G-time plot is equivalent to a 1/2 slope on a log-log Bourdet plot, and so for the ideal case, the method proposed by Mohamed et al. (2011) should be equivalent to the classical method for picking closure at the deviation from a straight line on a square root of time plot or a G-time plot. However, in many cases, as shown in Figure 2, two separate straight lines could plausibly be identified on the pressure versus G-function plot, and the $G \times \mathrm{d}P/\mathrm{d}G$ curve is almost continuously curving. The lower-left plot in Figure 17 shows the Bourdet plot with superposition derivative for the transient shown in Figure 2. The superposition derivative curve is almost continuously curving, and there is no clear

feature to support a pick of closure until the curve finally kinks over to a 1/2 slope at around 8 hours. Thus, the plot leads the interpreter to pick closure at the beginning of the 1/2 slope, which is equivalent to the beginning of the -1/2 slope on a conventional Bourdet plot with respect to Δt. The peak in the $\Delta t \times \mathrm{d}P/\mathrm{d}\Delta t$ curve (the point when the curve transitions from a 1/2 slope to a -1/2 slope) occurs at the same time as the peak in the $G \times \mathrm{d}P/\mathrm{d}G$ curve. Therefore, the Mohamed et al. (2011) method tends to give identifications of closure pressure that are similar to the conventional method of *G*-function interpretation, which is to draw a tangent to the $G \times \mathrm{d}P/\mathrm{d}G$ curve (leading to a closure pick near the peak of the curve).

1.2.3 Integrated pressure difference

Ramey and Agarwal (1972) showed that if fluid is instantaneously added or removed from a wellbore (a slug test), the pressure response can be written in terms of the derivative of the constant rate solution (the constant rate solution that is used must include the effect of wellbore storage). Peres et al. (1993) pointed out that this property can be applied for any reservoir geometry, and so pressure data from a slug test could be integrated to find the pressure change that would have occurred in response to constant rate production. Craig and Blasingame (2006) applied this method to analyze fracture-injection/falloff tests. If the hydraulic fracture is assumed to have formed instantaneously, the pressure data after shut-in can be integrated to find the effective pressure response, *I*. This can be written as:

$$I(\Delta P) = \int_0^{t_e+\Delta t} (P(\tau) - P_{init}) d\tau . \qquad (6)$$

This transformed pressure response can then be plotted on a Bourdet plot. For application to a DFIT test, the "wellbore storage" region on the Bourdet plot of integrated pressure has a very long duration because matrix permeability is very low and the storage includes both the wellbore and the fracture. Craig and Blasingame (2006) suggest identifying closure at the point where the fracture/wellbore storage changes (due to the changing fracture stiffness at closure). This corresponds to the time when a deflection can be identified during the wellbore storage period in the Bourdet plot with respect to integrated pressure.

Ribeiro and Horne (2013) tested this method on numerical simulations of hydraulic fracture initiation, propagation, and closure. Their simulations confirmed that closure could be picked at the point of deviation from the wellbore storage straight line from an integrated pressure Bourdet plot.

1.3 Summary of results

In this paper, we reexamine methods for picking closure in very low permeability formations and find that, in general, the closure pressure is incorrectly identified by several methodologies applied widely in the industry to interpret diagnostic fracture injection tests.

In contrast to the method originally proposed by Nolte (1991) and Barree and Mukherjee (1996), and used by many others since then, we find that a concave upward $G \times \mathrm{d}P/\mathrm{d}G$ curve is caused by the increasing fracture stiffness due to closure, and it is unnecessary to invoke stress heterogeneity and fracture height recession to explain this effect. Fracture height recession may

occur, but its effect is subtle compared to the dominant effect of closure on the pressure transient behavior. As a consequence, mechanical closure occurs earlier in the test and at a higher fluid pressure than predicted by traditional method. Figure 2 shows a field example, previously published by Cramer and Nguyen (2013). The traditional method for picking closure is to draw a line from the origin tangent to the $G\times \mathrm{d}P/\mathrm{d}G$ curve. Thus closure would be picked at around G-time of 36 and at a pressure around 49.3 MPa.

The method of Mohamed et al. (2011) for picking closure from Bourdet plots with superposition time generally gives similar answers as the traditional method of G-function plot interpretation, for the reasons described in Section 1.2.2. For the case shown in Figure 2, a detailed discussion is in given in Section 3.2. Closure often causes an upward deflection of the derivative curve, causing a slope slightly higher than 1.5. If closure picks were made at the point where that upward deflection occurs, the plot might be used to correctly pick closure. However, the upward deflection is visibly almost imperceptible or ambiguous, and so the closure pick is made near the start of the 0.5 slope for the derivative, which occurs at a time near the peak in the $G\times \mathrm{d}P/\mathrm{d}G$ curve and so at a similar time as predicted by the traditional method.

Our simulations show that under some conditions, the pressure change after shut-in can continue scaling with the square root of time *after* closure. This is equivalent to an increasing straight line on a pressure or $G\times \mathrm{d}P/\mathrm{d}G$ versus G plot, a 1/2 slope for $\Delta t\times \mathrm{d}P/\mathrm{d}\Delta t$ on a Bourdet plot, and a 3/2 slope for $\tau\times \mathrm{d}P/\mathrm{d}\tau$ on a Bourdet plot. This contradicts the assumption of Barree et al. (2007) that closure has not occurred if the $G\times \mathrm{d}P/\mathrm{d}G$ curve is continuing to rise (in low permeability formations) and also contradicts the method of Mohamed et al. (2011), who suggested that closure occurs at the end of the 3/2 slope on a log-log plot of $\tau\times \mathrm{d}P/\mathrm{d}\tau$.

We found that the Craig and Blasingame (2006) method of picking closure from the Bourdet plots with integrated pressure often identifies closure correctly. However, in many cases the plot is ambiguous to interpret. The deflection on the curve is very slight, and in some cases imperceptible. However, in principle, the method should pick closure correctly because it is designed to detect the initial change in fracture stiffness, which occurs at the moment of mechanical closure.

1.4 Proposed method for picking closure

Plots of pressure and $G\times dP/dG$ versus G-time (or alternatively, $t^5\times dP/dt^5$ versus the square root of time) are useful for picking closure because they facilitate identification of changes in the pressure derivative. However, we do not believe that closure should typically be picked near the top of the $G\times \mathrm{d}P/\mathrm{d}G$ curve, as is most often done today. The original concept of picking closure was to pick closure at the initial deviation from linearity on a plot of pressure versus G-time (Castillo, 1987). Equivalently, closure could be picked at the deviation from linearity on a plot of pressure versus the square root of time (Zoback, 2007). We advocate following these guidelines. Because of the residual aperture of the fracture, there may be a small stress shadow remaining when mechanical closure occurs. Therefore, the true minimum principal stress may be up to 1-2 MPa lower than the closure pressure (see discussion in Section 3.2). However, this difference is small and remains close to the experimental error of the test.

At very early time, there is a sharp drop in pressure caused by the disappearance of friction in the wellbore and near wellbore. This period should not be considered when picking closure pressure.

A linear period on the plot of P versus G should be visible after the end of this initial period. When closure occurs in low permeability formations, increasing fracture stiffness causes pressure to deflect downward and $G\times dP/dG$ to deflect upward, as discussed in Section 3.1.1.1. In high permeability formations, closure reduces the leakoff rate, and closure can cause pressure to deflect upward and $G\times dP/dG$ to deflect downward (though continue increasing), as discussed in Section 3.1.6. The $G\times dP/dG$ plot is useful for identifying closure because it makes it easy to identify these deflections.

Referring back to Figure 2, the first period of linearity on the pressure curve corresponds to a period when the $G\times dP/dG$ curve is also linear. Subsequently, the $G\times dP/dG$ curve deflects sharply upward. We believe that closure should be picked at the initial upward deflection, at a G-time of 7, corresponding to a pressure of about 55.2 MPa, much higher than the interpretation from the traditional method of picking closure when the $G\times dP/dG$ curve is tangent to a straight line drawn from the origin (Section 3.2). This interpretation also results in a much lower (and more plausible) estimate for the net pressure (bottomhole fluid pressure minus the minimum principal stress) at the ISIP. The upward curving shape of the $G\times dP/dG$ curve can be explained solely by increasing fracture stiffness with closure. It is not necessary to invoke fracture height recession or opening of transverse fractures to explain this observation. Additional data described in Section 3.2 suggests that these alternative explanations are unlikely for the case shown in Figure 2.

Undoubtedly, there are cases too complex to be handled with our proposed guidelines. However, our proposed method should be sufficient for a large percentage of DFIT cases. Our modeling results show that DFITs interpretations are often unnecessarily complex. Our results show the value of interpreting DFITs with a numerical simulation tool that properly sets up and solves the equations that describe the key physics. In Section 2.2, we discuss the difference between the model used in this study and other models that have been used in the literature.

1.5 Residual fracture aperture

The key difference between our work and most prior work on this topic is that we consider the effect of residual aperture on fluid storage after mechanical closure. We use a three-dimensional hydraulic fracture simulator that rigorously solves the hydromechanically coupled problem of fracture initiation and closure. When fracture walls come into contact, the simulator switches to a non-linear joint closure law based on the work of Barton et al. (1985), which allows the fracture to remain hydraulically conductive and continue to store fluid after mechanical closure has occurred. This is similar to the approach used by Plahn et al. (1997) and Ribeiro and Horne (2013).

There is abundant evidence to suggest that fractures retain storativity and conductivity after the walls have come into contact (mechanical closure). Fractures retain aperture after mechanical closure due to mismatch of asperities in the fracture walls. An extensive literature exists on the relationship between fracture aperture, conductivity, fluid pressure, and stress (Gangi, 1978; Witherspoon et al., 1980; Walsh, 1981; Barton et al., 1985; Brown and Bruhn, 1998; Pyrak-Nolte and Morris, 2000). It is almost impossible to know exactly how much fracture surface roughness is generated when a hydraulic fracture is formed during a DFIT and to what degree the asperities mismatch after closure. However, it is certain that they retain aperture and ability to conduct fluid because the -1/2 slope pressure transients frequently observed in Bourdet plots of DFIT

data can only occur if there is a post-closure infinite conductivity fracture. In high permeability formations, the fluid storage and conductivity retained post-closure quickly becomes negligible. But in very low permeability formations, leakoff into the matrix is very slow, and so even fracture apertures of 10s-100s of microns can have a dominant effect on the pressure transient.

The dimensionless fracture conductivity (or equivalently, dimensionless fracture transmissivity) is defined as:

$$C_{fD} = \frac{T}{kL_f}, \tag{7}$$

where T is the fracture transmissivity, k is the matrix permeability, and L_f is the fracture half-length. A fracture will behave like an infinite conductivity fracture as long as $C_{fd} > 300$. From the cubic law (Witherspoon et al., 1980), the fracture transmissivity is defined as:

$$T = \frac{e^3}{12}. \tag{8}$$

For a fracture with half-length of 50 m and matrix permeability of 10^{-19} m^2 (~100 nanodarcies), the fracture will be infinite conductivity as long as fracture aperture is greater than just 26 microns.

Our results suggest that in DFITs, the fracture retains significant fluid storage at the moment of mechanical closure, on the order of 100s of microns. Otherwise, closure would result in an excessively rapid drop in fluid pressure (with a spike in the pressure derivative), more rapid than is typically observed. Other authors in the literature have reported calculations that predict sharp drops in pressure upon fracture closure (Koning and Niko, 1985; van den Hoek, 2002; Ribeiro and Horne, 2013). However, in field data, the increase in derivative at closure is more gradual. In our simulations, we found that as long as the fracture retains hundreds of microns of residual aperture upon closure (this could be due to both microscopic asperities and also macroscopic roughness and non-planarity of the fracture), the discontinuity in derivative at closure does not occur and simulations can be performed that closely match field data.

2. Methods

2.1 Details of the numerical simulation code

The numerical simulations were performed using CFRAC (Complex Fracturing ReseArch Code), which fully couples fluid flow with the stresses induced by fracture deformation in discrete fracture networks (McClure and Horne, 2013; McClure et al., 2015). CFRAC can describe complex fracture networks, but all simulations described in this paper assumed a single planar fracture perpendicular to the minimum principal stress. The simulations were fully 3D, with the fractures discretized into square elements in the vertical and horizontal directions.

The fluid flow equations are solved fully implicitly using the finite volume method. Timestep duration is chosen adaptively. The fluid is single phase, single component, constant compressibility (c_f), constant viscosity (μ), and has initial density of ρ_{init}. The simulations are isothermal and the effect of gravity is neglected. The simulations are initialized with homogeneous stress and fluid pressure. The stress calculations assume the fractures are

embedded in an elastic half-space (though typically the depth is so great relative to fracture size that the depth has negligible effect on the simulation).

Within the fracture, the unsteady state mass balance equation is solved with Darcy's law:

$$\frac{\partial(E\rho)}{\partial t} = -\nabla \cdot \left(q_{flux} e\right) - q_{m,leakoff,a} + s, \tag{9}$$

$$q_{flux} = -\rho \frac{k}{\mu} \nabla P, \tag{10}$$

where E is the void aperture (the volume of fluid stored per surface area of fracture), ρ is fluid density, t is time, q_{flux} is the (vector valued) mass flux of fluid through the fracture, e is the hydraulic aperture (the effective thickness of the fracture available for flow, which is assumed to be equal to void aperture in the simulations in this paper), $q_{m,leakoff,a}$ is the mass rate of leakoff per fracture surface area into the surrounding matrix (described in Section 2.1.5), s is a source term representing a well, k is the fracture permeability, μ is fluid viscosity, and P is fluid pressure.

The permeability of the fracture is defined to be equal to:

$$k = \frac{e^2}{12}. \tag{11}$$

When permeability is multiplied by hydraulic aperture, the result is the transmissivity, T, and the classical cubic law results (Equation 8).

Non-linear relationships are used to relate pressure, stress, and deformation to aperture. We define a "closed" fracture as a fracture where the fluid pressure is less than the normal stress and the walls of the fracture are in contact. Roughness of the fracture walls allows closed fractures to retain hydraulic and void aperture. We define an "open" fracture as a fracture where the fluid pressure has reached the normal stress and the walls are no longer in contact. For the simulations in this paper, the void aperture and the hydraulic aperture were assumed to be equal.

The aperture of closed fracture elements was estimating using the following joint closure relation, which was written in this form by Willis-Richards et al. (1996), based on the work of Barton et al. (1985):

$$E = \frac{E_0}{1 + 9\sigma_n^{'} / \sigma_{n,ref}}, \tag{12}$$

where E_0 is the residual aperture (the aperture at effective stress equal to zero), and $\sigma_{n,ref}$ is the 90% closure stress. The fracture effective normal stress, σ_n', is equal to the normal stress, σ_n, minus fluid pressure.

For open elements, the aperture is defined as:

$$E = E_0 + E_{open}, \tag{13}$$

where E_{open} is the mechanical separation between the fracture walls.

A special algorithm is used to define the value of E_0 for hydraulic fractures. When a hydraulic fracture element first initiates in CFRAC, it is given a very small aperture (in this study, the initial aperture was 0.1 microns). But the residual aperture of a fully open fracture should be on the order of 10s or 100s of microns. To solve this problem, an algorithm is used that allows E_0 to increase as the fracture opens. The algorithm mimics the natural process of fracture roughness development as the crack initiates and opens. The algorithm sets E_0 of each element to be equal to 90% of the maximum aperture reached by the element. Thus, E_0 can increase, but never decrease. In our previous work on DFIT analysis (McClure et al., 2014), a maximum value of E_0 was not specified. In this study, a maximum value on E_0 was used, $E_{hf,max,resid}$.

Arithmetic averaging is used to calculate the average transmissivity for flow between two elements that have different transmissivity. Wellbore storage is included, as described by McClure et al. (2014), and is parameterized by the wellbore storage coefficient, C_w, which has units of volume per unit pressure.

Fluid leakoff is calculated assuming that the reservoir is slightly compressible with compressibility c_ϕ, initial porosity of ϕ_{init}, and contains the same fluid as the injection fluid (this latter assumption is necessary because the simulator is single phase, single component). Leakoff is assumed to be one-dimensional away from the fracture, a reasonable assumption in very low permeability formations unless the transient is very long in duration (Gringarten et al., 1974). Often, leakoff from fractures is modeled in the literature with the one-dimensional Carter leakoff model (Howard and Fast, 1957). However, the Carter leakoff model calculates leakoff rate assuming that fluid pressure in the fracture is constant with time. During DFITs, large pressure changes occur, and so the Carter leakoff model is not appropriate. Instead, we use the semi-analytical method of Vinsome and Westerveld (1980), which also assumes 1D leakoff, but accurately accounts for changing pressure in the fracture over time.

Poroelastic stress changes in the fracture due to flow in the matrix are neglected. Also, poroelastic pressure response in the matrix due to fracture deformation is neglected. Poroelastic stress effects on the fracture are not typically considered for DFIT analysis (Nolte, 1979; Barree and Mukherjee, 1996). In a typical DFIT (very low permeability), the region of pressure increase around the fracture is very narrow, and so the poroelastic effect of stress on the fracture is slight. This can be seen from Equation 1 provided by Perkins and Gonzalez (1985), who gave an expression for the induced change in normal stress on a fracture due to an ellipsoidal region of cooling around the fracture. They provided a result for thermal stress, but the result is directly analogous to poroelastic stress. Their equation shows that for a long and narrow region of cooling, the normal stress induced on the fracture is negligible. This result can analogously be obtained from the analytical solution for the stresses induced by a rectangular cuboid region of thermal perturbation provided by Nowacki (1986) or from numerical calculations, as discussed by McClure and Horne (2010). Wallace et al. (2014) investigated the effect of poroelastic stresses on DFITs and found only a very slight effect.

The mechanical calculations are performed assuming that the formation is mechanically homogeneous, isotropic, and linearly elastic. The calculations are performed using the boundary element method of Okada (1992), which uses constant displacement, rectangular elements in an elastic half-space. This method satisfies the equations of quasi-static stress equilibrium, Hooke's law, and compatibility, giving results that are convergent with mesh refinement to exact analytical solutions from classical fracture mechanics (Babazadeh and McClure, 2015).

For a mechanically open element, the condition is enforced that:

$$\sigma_n^r - P + \Delta\sigma_n = 0, \tag{14}$$

where σ_n^r is the normal stress on the fracture due to remote loading (calculated from the initial conditions) and $\Delta\sigma_n$ is the change in normal stress due to stress induced by the cumulative deformation of all the fracture elements in the system, as calculated from the Okada (1992) method. In the fully implicit solver, Equation 14 is solved simultaneously with Equation 9.

Closed elements experience small normal displacements in response to changes in effective normal stress (Equation 12). The stress changes due to these aperture changes were included in the simulations using the method described in Sections 2.2.3 and 2.2.4 of McClure and Horne (2013).

Fracture initiation occurs at the wellbore when the fluid pressure reaches the minimum principal stress. Propagation is handled using linear elastic fracture mechanics. The stress intensity factor at the crack tips (vertically and horizontally) is calculated using the equation given by Olson (2007):

$$K_I = 0.806\left(\frac{2G_m\sqrt{\pi}}{4(1-\upsilon)\sqrt{a}}\right)E_{open}, \tag{15}$$

where G_m is the shear modulus, υ is Poisson's ratio, and a is the half-length or half-height of the element (we used square elements). If the stress intensity factor reaches the fracture toughness, K_{Ic}, the fracture extends by one element.

Fracture height confinement can occur due to differences in stress between layers. The code is capable of including stress heterogeneity and simulating the effect of stress layering on height confinement. However, for simplicity, in the simulations for this paper, the fracture height was assumed to be limited to no more than 7 m. The only exception was Simulation G1, in which no height confinement was assumed and the fracture propagated radially.

The wellbore and near wellbore pressure drop is modeled as being proportional to the square of the flow rate from the wellbore to the formation:

$$\Delta P_{nw} = C_{nw}Q^2, \tag{16}$$

where C_{nw} is a constant and Q is the volumetric flow rate from the wellbore to the formation. This term combines the effect of friction in the wellbore, the perforations, and the near wellbore region. The perforation pressure drop is a function of the number of flowing perforations, the perforation diameter, and the perforation shape (Cramer, 1987). Friction in the wellbore is related to wellbore diameter and the wellbore roughness (Moody, 1944).

Typically, the pressure drop associated with injection through well tubulars and perforations during DFIT treatments is very small, especially when the injection rate is 2 bbl/min or less. An often-significant pressure drop is indeed located near the wellbore but is more typically downstream of the perforations: (1) along a tortuous flow path from the perforations to the primary fracture and/or (2) due to the interaction of multiple (short) fractures of different

orientations (longitudinal, multiple transverse orientations, horizontal) which is set up as the result of near-wellbore stress concentration, e.g., hoop stress.

In cases of large near-wellbore pressure drop (due to perforation friction, tortuousity or multiple fracture interaction, singly or in combination), the incremental fluid compression associated with the injection-induced overpressure must dissipate before the response of the closing primary fracture is observable. Wellbore storage volume, the magnitude of the overpressure, fluid leak-off rate and post-injection fracture extension are among the factors determining the time necessary to dissipate the excess pressure.

2.2 Comparison to other models

A variety of other models have been applied to simulate DFITs. It is worthwhile to mention key differences.

Some models have described the fracture formed during injection with a continuum approach. Meng et al. (2014) and Padmakar (2013) represented a DFIT as creating a single fracture, but treated the fracture as a thin layer within the porous medium with different properties (such as permeability) than the surrounding formation. Wallace et al. (2014) modeled the fracture with a dual porosity approach.

To model the process of fracture closure in detail, it is most realistic to use a discrete fracture approach. Mathematically, fractures are opening mode displacement discontinuities (Crouch and Starfield, 1983). Solving for the opening distribution along a crack requires imposing the appropriate boundary condition: that fluid pressure equals normal stress (Equation 14), which arises directly from the requirement of force equilibrium (Crouch and Starfield, 1983). In hydraulic fracture problems, this equation must be coupled with fluid flow. This is the approach used in classical papers such as Sneddon (1946), Khristianovic and Zheltov (1959), Perkins and Kern (1961), Geertsma and de Klerk (1969), Nordgren (1972) and in conventional hydraulic fracturing simulators.

Barree and Mukherjee (1996) simulated DFITs with a hydraulic fracturing simulator that explicitly represented the fracture as an opening mode displacement discontinuity, a similar approach to the present work. Their paper explained and proposed many concepts for non-ideal DFIT behavior that have been developed by many authors since Nolte (1991): fracture height recession, pressure dependent leakoff, transverse fracture storage, and tip extension. Barree and Mukherjee (1996) used the 3D hydraulic fracturing simulator GOHFER (Barree, 1983). Barree (1983) did not describe how GOHFER handles fracture aperture after closure, but we believe that it assumes aperture goes to zero after closure.

Ribeiro and Horne (2013) modeled diagnostic injection tests tests with a hydraulic fracturing simulator. They permitted the fractures to have residual aperture after closure. Consistent with the findings from this study, they found that the pressure derivative increased sharply upon closure.

Plahn et al. (1997) modeled pumpin/flowback tests with a numerical fracturing model that allowed fractures to retain residual aperture, similar to the model presented in this work. They

did not investigate pumpin/shut-in tests, but consistent with our findings, they found a sharp increase in the pressure derivative when closure occurred.

2.3 Comparison to analytical approaches

Several authors have used analytical approaches to describe pressure transient behavior during mechanical closure in diagnostic injection tests (Craig and Blasingame, 2006) or after shut-in of a hydraulically fractured water injection well (Koning and Niko, 1985; van den Hoek, 2002). Consistent with our findings, Koning and Niko (1985) and van den Hoek (2002) found that an increase in the pressure derivative should occur upon closure. However, they used simplified treatments of fracture compliance after closure and predicted an exaggerated spike in derivative (as shown in our simulations in Section 3.1.1). Also, they were not focused specifically on understanding the consequences for closure identification.

Raaen et al. (2001) described pump-in/flow-back tests and pump-in/shut-in tests in terms of "system stiffness." Consistent with our findings, they described how the magnitude of the pressure derivative should increase with closure due to the increasing fracture stiffness. However, Raaen et al. (2001) neglected the effect of residual fracture aperture on storage after closure (as described in Appendix A) and primarily focused on pump-in/flow-back tests.

3. Results and discussion

In the following sections, a variety of simulation results are presented and discussed. In Section 3.1, a series of generic simulations are performed in order to investigate the effect of different physical processes on pressure transient behavior. Simulation results are compared to analytical solutions to validate our modeling approach. In Sections 3.2, 3.3, and 3.4, results are provided to match field datasets: Field DFIT #1, #2, and #3. Field DFIT #1 is nearly ideal, and so an almost perfect match to the data was possible. Field DFITs #2 and #3 involve a greater degree of complexity, and so very close matches were not possible (nor were they attempted). However, the simulations replicate the key features of the transients. In Section 3.5, we provide data from the GRI/DOE M-site field demonstration project. At this site, hydraulic fracture injections were performed in conjunction with downhole tiltmeter measurements that provided an independent estimate of the closure pressure. In Section 3.6, we discuss nonuniquness and describe which model parameters were well-constrained by the data and which were not. In Section 3.7, we discuss the possibility that pump-in/flow-back tests could be performed subsequent to DFIT tests in order to provide an independent measurement of the minimum principal stress.

Table 1: Simulation settings used in all simulations. See Section 3.6 for discussion on the selection of these parameters.

υ (unitless)	0.25
μ (cp)	1
c_f (MPa^{-1})	0.000458
ρ_{init} (kg/m^3)	1000
c_ϕ (MPa^{-1})	0.00145
ϕ_{init} (unitless)	0.03

Table 2: Differences in simulation settings between different simulations. See Section 3.6 for discussion on the selection of these parameters.

	G1	G2	G3	G4	G5	G6	F1	F2	F3
G_m (GPa)	15	15	15	15	15	15	15	7.5	7.5
P_{init} (MPa)	35	35	35	35	35	35	33.7	64.35	66.7
$E_{hf,resid,max}$ (mm)	0.001	0.001	0.5	0.5	0.5	0.5	0.5	0.5	0.5
K_{1c} (MPa-m$^{1/2}$)	10	10	10	10	2	2	4	1	1
Maximum fracture height (m)	Unconfined	7	7	7	7	7	7	7	7
$\sigma_{n,ref}$ (MPa)	51	51	51	5	5	5	17	50	10
σ_{hmin} (MPa)	55.1	55.1	55.1	55.1	55.1	55.1	54.3	77.06	83.5
C_w (m^3/MPa)	0	0	0	0.0184	0.0184	0.0184	0.0184	0.0256	0.0146
Injection rate (kg/s)	13.25	13.25	13.25	13.25	13.25	13.25	variable; max of 13.25	2.187	4.845
Injection duration (s)	120	120	120	120	120	120	352	496	592.2
k (m^2)	10^{-19}	10^{-19}	10^{-19}	10^{-19}	10^{-19}	10^{-15}	6×10^{-20}	3×10^{-22}	2×10^{-19}
C_{nw} (MPa/(m^3/s)^2)	0	0	0	3.3×10^4	3.3×10^4	3.3×10^4	2.2×10^4	6.8×10^6	6.8×10^5

3.1 Generic simulations

In this section, a series of generic DFIT simulations are presented. The simulations were designed to demonstrate the effect of different physical processes. The settings that were used in the simulations are given in Table 1. The differences in settings between simulations are given in Table 2.

Superposition time, τ, and G-time are calculated as functions of time of shut-in, Δt, and the duration of injection, t_e. Prior to the leakoff point, injected fluid is almost entirely stored in the wellbore and leakoff into the formation is negligible. To account for this, t_e was defined to be equal to the duration of injection after the leakoff point was reached, rather than the entire duration of injection.

3.1.1 Simple baseline simulations

Simulation G1 assumed a radial fracture geometry (no height containment) with no wellbore storage, very small residual aperture, and fairly high fracture toughness. Simulation G2 was similar to Simulation G1, but the hydraulic fracture was assumed to be confined in height to 7 meters. Figure 4 and Figure 5 show the results from Simulations G1 and G2. For calculating t_e, the "leakoff point" in Simulations G1 and G2 occurred immediately at the start of injection because there was not any wellbore storage.

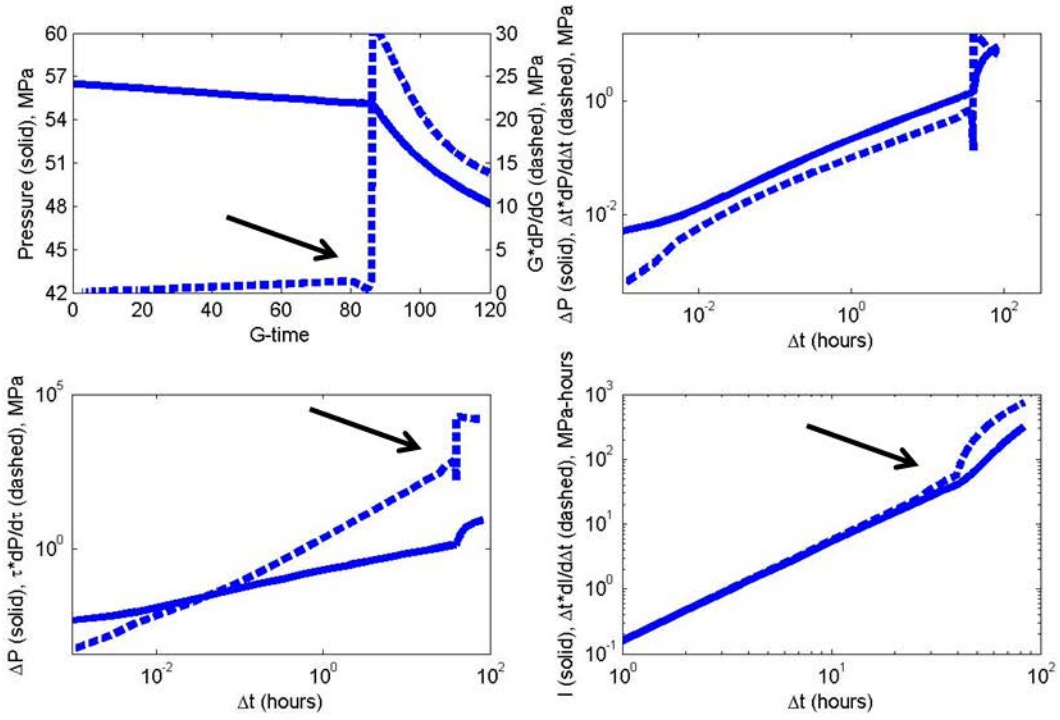

Figure 4: Results from Simulation G1. Upper left: G-function plot. Upper right: Bourdet plot with derivative with respect to time. Lower left: Bourdet plot with derivative with respect to superposition time. Lower right: Bourdet plot with integrated pressure (zoomed in).

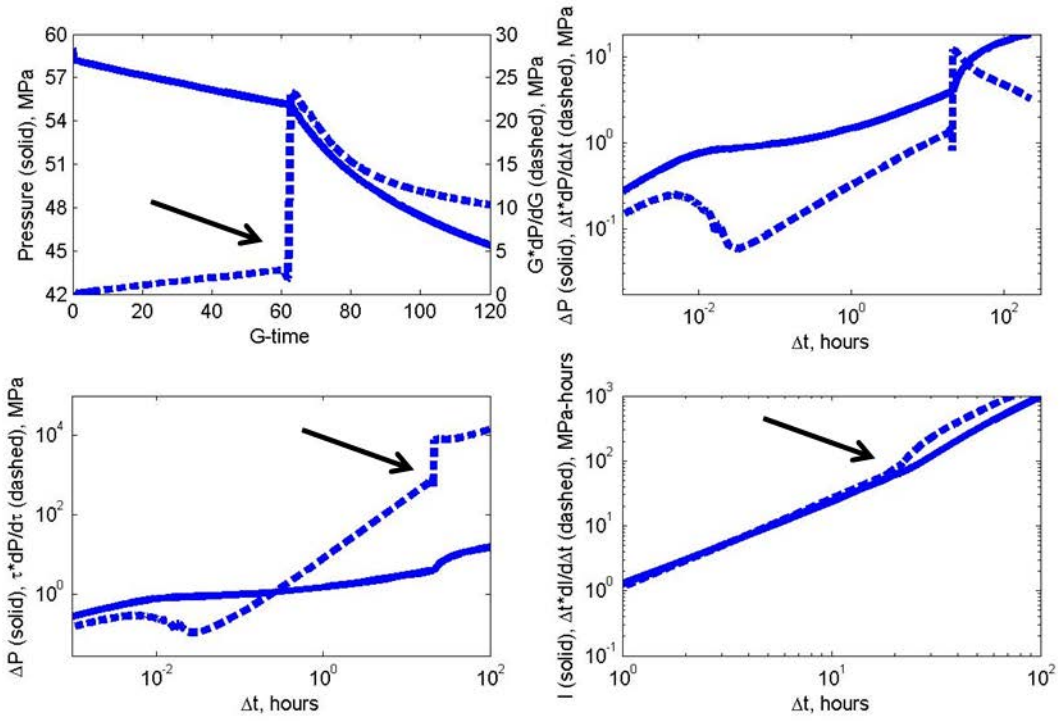

Figure 5: Results from Simulation G2. Upper left: *G*-function plot. Upper right: Bourdet plot with derivative with respect to time. Lower left: Bourdet plot with derivative with respect to superposition time. Lower right: Bourdet plot with integrated pressure (zoomed in).

Simulations G1 and G2 had a very sharp (unrealistic) spike in derivative when closure occurred. Closure clearly and unambiguously occurred in the pressure transient at a fluid pressure equal to 55.1 MPa, precisely the same as the minimum principal stress assumed in the simulation. Closure can clearly be identified in all four plots.

3.1.1.1 Stiffness contrast at closure

In Appendix A, a detailed derivation is provided for the equations governing a DFIT pressure transient. After shut-in and the period after shut-in when flow rate dependent pressure gradients dissipate, it is shown that:

$$\frac{dP}{dt} = \frac{-q_{leakoff}}{c_f V_{wl} + \dfrac{A}{S_f}}, \tag{17}$$

where c_f is the compressibility of the fluid, V_{wl} is the volume of the well, A is the surface area of the fracture, and S_f is the fracture stiffness. The fracture stiffness can be defined in several equivalent ways: the derivative of effective normal stress with respect to fracture closure (fracture closure being equal to negative change in aperture), the negative of the derivative of effective normal stress with respect to aperture, or the reciprocal of the derivative of aperture with respect to pressure (Chapter 12 from Jaeger et al., 2007). Equation 17 neglects the effect of

the compressibility of the fluid in the fracture and the effect of the changing wellbore volume because both terms are of negligible magnitude in typical DFIT applications.

The derivation of Equation 17 is similar to the "system stiffness" approach described by Raaen et al. (2001), except that Raaen et al. (2001) implicitly assumed that fracture volume is zero after closure. The denominator of Equation 17 is equivalent to the "before closure" storage coefficient defined by Craig and Blasingame (2006). However, Craig and Blasingame (2006) assumed that after closure, the fracture aperture is constant (equivalent to infinite fracture stiffness), and defined a separate "after closure" storage coefficient. In contrast, we find that Equation 17 applies for the entire shut-in period. When closure occurs, the value of S_f changes, which has the critical effect on the pressure transient.

For a radial fracture, the stiffness of an open fracture (defined as $S_{f,o}$) can be written as (Sneddon, 1946):

$$S_{f,r} = \frac{3\pi G_m}{8(1-\nu)R_f}, \tag{18}$$

where G_m is the shear modulus, υ is Poisson's ratio, and R_f is the radius. For a fracture with length much longer than its height, the stiffness can be estimated using the PKN assumption of plane strain in vertical cross-section (Sneddon, 1946; Perkens and Kern, 1961; Nordgren 1972):

$$S_{f,PKN} = \frac{4G_m}{\pi(1-\nu)h_f}, \tag{19}$$

where h_f is the fracture height.

Prior to closure, the leakoff rate scales with time according to the *G*-function (Nolte, 1979) and the denominator of Equation 17 is constant, which is why a plot of pressure versus *G*-time forms a straight line.

In Appendix A, the stiffness of a closed fracture is derived (in analogy to the discussion in Chapter 12 from Jaeger et al., 2007):

$$\frac{d\sigma_n'}{dE} = S_{f,c} = S_{f,o} + S_{f,cont}, \tag{20}$$

where $S_{f,c}$ is the stiffness of a closed fracture and $S_{f,cont}$ is the contribution to the stiffness from the contacting of the fracture walls. It can be calculated from a constitutive law that relates aperture to effective normal stress (such as Equation 12) by solving for effective normal stress and then taking the derivative with respect to aperture:

$$S_{f,cont} = \frac{\sigma_{n,ref}}{9}\frac{E_0}{E^2} = \frac{\sigma_{n,ref}}{9E_0}\left(1+\frac{9(\sigma_n - P)}{\sigma_{n,ref}}\right)^2. \tag{21}$$

In Simulation G1, the fracture was circular. The radius at shut-in was 21 m, but the fracture extended slightly after shut-in and reached a final radius of 21.6 m. From Equation 18, the pre-closure stiffness was 1.09 MPa/mm. From Equation 19, the pre-closure stiffness in Simulation G2 (which had fracture height of 7 m) was 3.64 MPa/mm.

Equation 21 shows that two parameters: E_0 and $\sigma_{n,ref}$, affect the contact stiffness at the moment of closure. In order to avoid a sharp discontinuity in stiffness and the pressure derivative, the stiffness at mechanical closure cannot be much greater than the stiffness prior to closure.

3.1.1.2 Laboratory verification of fracture apertures

In Simulations G1 and G2, the residual aperture was set to 10 μm and $\sigma_{n,ref}$ was set to 51 MPa. Therefore, the stiffness due to contact at closure was 567 MPa/mm, orders of magnitude greater than the pre-closure stiffness. This is why there was an unrealistically large discontinuity in derivative. Other authors have discussed the impact of stiffness contrast at closure, and also described a spike in derivative upon closure (Koning and Niko, 1985; Raaen and Brudy, 2001; van den Hoek, 2002; Craig and Blasingame, 2006; Riberio and Horne, 2013).

Laboratory tests give some insight into reasonable values for E_0 and $\sigma_{n,ref}$. Barton et al. (1985) tested aperture as a function of normal stress in joints from a variety of rock types. As joints were compressed from normal stress of zero to 20 MPa, Barton et al. (1985) reported total aperture changes in the range of 70 μm to 500 μm. They found that the roughness of the fracture walls was the most important factor in determining E_0. Barton et al. (1985) also reported that aperture changes exhibited hysteresis, experiencing the greatest aperture decrease with compression on the first loading cycle, with lower aperture change for subsequent loading cycles. This raises the interesting possibility that hydraulic fractures may exhibit greater E_0 and lower $\sigma_{n,ref}$ when they close for the first time than in subsequent injection/leakoff cycles.

Zhang et al. (2013) tested fracture conductivity as a function of effective normal stress for a variety of fractures taken from outcrops of the Barnett shale. They measured fracture conductivity as a function of effective normal stress but did not measure aperture or conductivity at effective normal stress of zero. The results varied considerably, depending on whether the joint was naturally formed, the infilling in the joint, and whether the walls were offset. In one experiment (Figure 15 from Zhang et al., 2013), they induced a fracture in a sample and then carefully ensured that the walls were not displaced by shear, which would mismatch asperities and increase aperture. Their results showed a very sharp decrease in conductivity with increasing normal stress. They reported conductivity of 45, 3.5, and 0.3 mD-ft at normal stress of 200, 500, and 1000 psi respectively. Using the cubic law, these conductivities correspond to apertures of 56 μm, 24 μm, and 11 μm, respectively. Extrapolating the non-linear trend in their data, the fracture conductivity at effective stress of zero can be estimated to be 300 mD-ft, equivalent to an aperture of 106 μm. The values suggest that the 90% closure stress of the joint was on the order of 1000 psia (6.9 MPa). In another sample under the same conditions (Figure 16 from Zhang et al., 2013), conductivity at 200 psi was 500 mD-ft. This data would extrapolate to perhaps 2000 mD-ft at effective normal stress of zero, equivalent to an aperture of 200 μm.

Thus, laboratory experiments indicate that residual aperture can be on the order of 100s of microns and that $\sigma_{n,ref}$ can be at least as low as 5-10 MPa.

In field-scale hydraulic fracturing, macroscopic roughness, non-planarity, and complexity could increase residual aperture above what is observed in laboratory scale experiments. Multiple fracture strands, branching, and non-planarity, which are widely observed in direct observations of hydraulic fracture geometry (Warpinski and Teufel, 1987; Mahrer, 1999), would tend to

increase the stiffness of the fracture pre-closure, compared to the idealized radial and PKN geometries. Therefore, simplifications involved in using assuming idealized fracture geometry and measuring fracture properties in the lab will tend to bias our calculations towards predicting greater stiffness contrast at closure than will actually occur in the subsurface.

3.1.1.3 Comparison to analytical solutions

As summarized by Marongiu-Porcu et al. (2011), the pressure trend prior to closure can be used to estimate the leakoff coefficient and the fracture size (Nolte, 1979; Shlyapobersky et al., 1988; Valko and Economides, 1999). The technique involves drawing a straight line through the plot of pressure versus *G*-time during the pre-closure period.

In Simulation G1, the slope of the line was -0.0166 MPa/*G* with an intercept of 56.51 MPa, and the fracture had radial geometry. This yields an estimate of fracture radius of 20.4 m (using the value of plane strain modulus, E', of 40 GPa, which can be derived from the values of shear modulus and Poisson's ratio in Table 1). In the simulation, the actual radius at shut-in was 21 m, and a bit of additional propagation occurred so that the final radius was 21.6 m. Using the final value of radius in the simulation, 21.6 m, the equations yield an estimate of leakoff coefficient of 6.95×10^{-7} m/s. From Howard and Fast (1957), $C_L = \Delta P\sqrt{\frac{k\phi c_t}{\pi\mu}}$. Assuming a value of ΔP equal to 56.51 - 35 = 21.51 MPa, the true value of C_L was 9.18×10^{-7} m/s, close to the estimated value, though somewhat larger. The modest discrepancy is perhaps unsurprising because the derivation of these *G*-function-based methods relies on several assumptions, such as Carter leakoff and power-law growth of the fracture, that are unlikely to be exactly satisfied by our more general numerical calculations. Using the true values of radius at shut-in (21 m) and leakoff coefficient, the analytical equation predicts an average fracture aperture of 1.12 mm, compared to the actual value from the simulation value of 1.11 mm. Using the actual simulation values of average aperture and radius at shut-in, the analytical equation predicts efficiency (volume of fluid in the fracture divided by volume injected) at shut-in of 97%, exactly the same as the actual efficiency at shut-in during the simulation.

In Simulation G2, the slope of the line was -0.0496 MPa/*G* with an intercept of 58.19 MPa. Using the equations for a PKN fracture, this yields an estimate of fracture half-length of 133.7 m. At shut-in, the actual fracture half-length was 108.6 m. The fracture propagated a bit further after shut-in, reaching 122.6 m. Using the actual value of final fracture half-length, the analytical equation predicts leakoff coefficient of 6.95×10^{-7} m/s. Using actual values of half-length at shut-in and leakoff coefficient, the analytical expressions predict average aperture of 1.02 mm, compared to the actual simulation value of 1.01 mm. Using the actual value of average aperture and fracture half-length at shut-in, the analytical expression predicts efficient at shut-in of 97%, the same as the actual efficiency at shut-in during the simulation.

3.1.2 Effect of increasing residual aperture

Simulation G3 was a PKN-like simulation (height confined to 7 m), identical to Simulation G2, except that the fracture was given a maximum residual aperture of 500 microns. The results are shown in Figure 6.

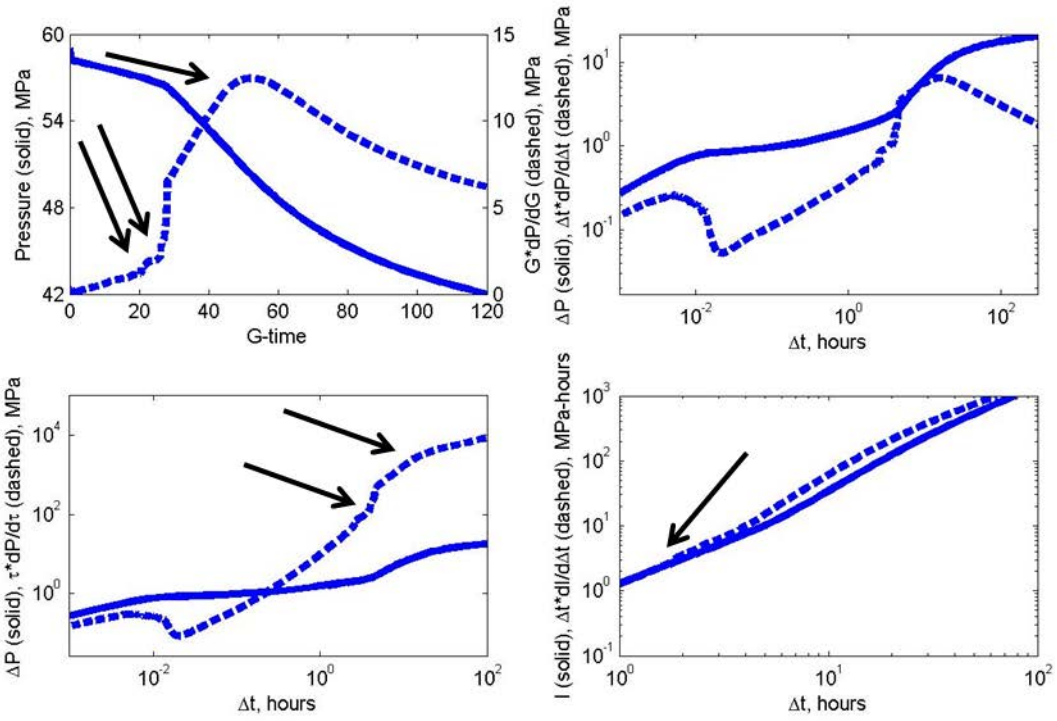

Figure 6: Results from Simulation G3. Upper left: *G*-function plot. Upper right: Bourdet plot with derivative with respect to time. Lower left: Bourdet plot with derivative with respect to superposition time. Lower right: Bourdet plot with integrated pressure (zoomed in).

A discontinuity in the derivative of pressure still occurred when closure occurred, but it was much less pronounced than in Simulations G1 and G2. The 90% closure stress was 51 MPa, and so the stiffness at closure due to contact was 11.3 MPa/mm, only a factor of three greater than the stiffness of the fracture pre-closure.

In this paper, we propose that closure should be picked at the upward deviation of the $G \times dP/dG$ curve. In Simulation G3, this occurred at either *G*-time of about 20 (2.4 hours), and a pressure equal to 57 MPa or at *G*-time of 25.5 (3.8 hours) and a pressure equal to 56.6 MPa.

The traditional method would pick closure from the *G*-function plot at *G*-time equal to about 46, equivalent to about 12 hours. This would yield an estimate of closure pressure equal to about 51.8 MPa. In the Bourdet plot with superposition derivative, there appears to be a 1.5 slope, followed by a disturbance in the derivative at around the time of closure, followed by what appears to be a resumption of the 1.5 slope until about 12 hours. Picking closure at the end of the second 1.5 slope would yield a closure estimate similar to the traditional method, about 51.8 MPa. Picking closure at the end of the first 1.5 slope would yield a result close to our proposed method.

In the Bourdet plot with integrated pressure, an upward deflection of the derivative plot can be seen as early as 1.7 hours after shut-in, equivalent to *G*-time of 16.7, giving a closure pick of 57.2 MPa. Because the Bourdet plot with integrated pressure picks closure at the first indication of a change in fracture stiffness, it tends to give a closure pick closer to our proposed method.

From the simulation results, it is possible to identify when and how mechanical closure occurred. Figure 7 shows the distribution of aperture and residual aperture in the fracture shortly after shut-in. The red lines represent the residual aperture and the blue lines represent the aperture. The upper part of the figure shows the aperture distribution along the fracture length, down the midpoint. The lower part of the figure shows the aperture distribution along a vertical line running through the center of the fracture.

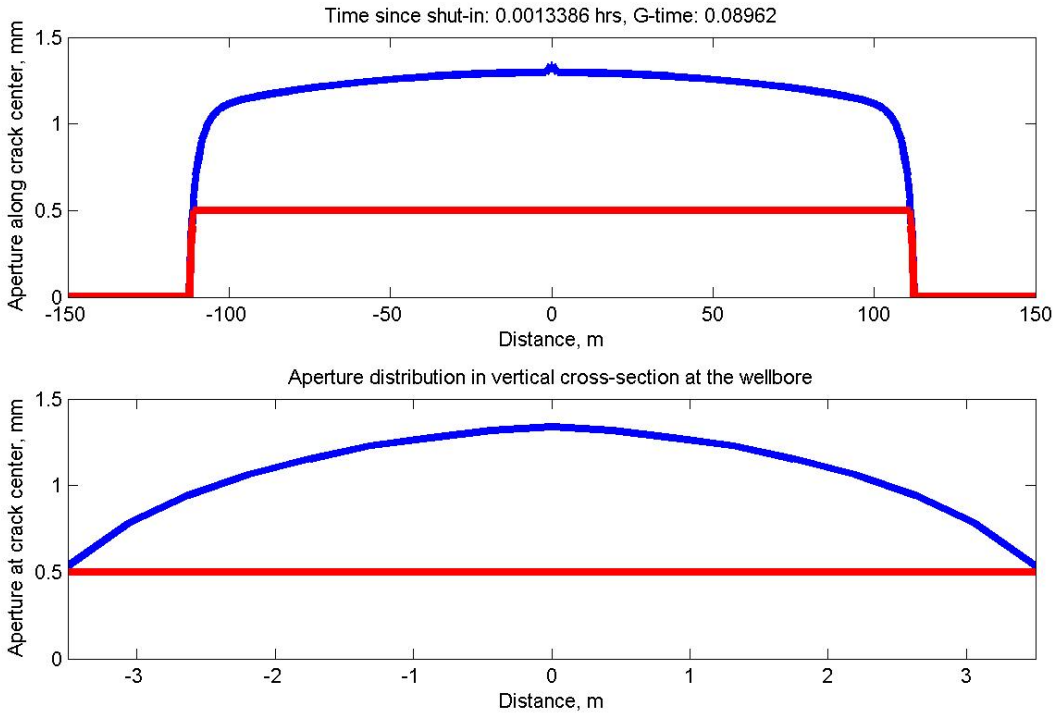

Figure 7: Distribution of aperture during Simulation G3 shortly after shut-in. The upper figure shows aperture along the length of the fracture and the lower figure shows aperture along a vertical cross section at the center of the crack.

Figure 8 shows the aperture distribution after 2.32 hours of shut-in. Here, it can be seen that while the fracture had not closed along its length, a fracture height recession process had begun to occur. The fracture had closed to the residual aperture along the upper and bottom 1.5 m of the fracture. The beginning of this fracture height recession process is what caused the initial slight discontinuity and increase in the derivative at *G*-time equal to about 20.

The height recession was not due to stress layering in the formation (stress was homogeneous). Instead, height recession was caused by the residual aperture. As predicted by the PKN approximation, the aperture distribution in the vertical direction was elliptical, tapering to zero at the edges (though this was imperfectly captured in the simulation because of mesh coarseness). The maximum residual aperture was specified to be a constant value, 500 microns. As the fluid pressure decreased, aperture gradually decreased, maintaining an elliptical shape and continuing to taper to zero at the top and bottom. As aperture decreased, regions developed where the aperture had reached the residual aperture (mechanical closure). These regions extended inward from the top and bottom of the fracture.

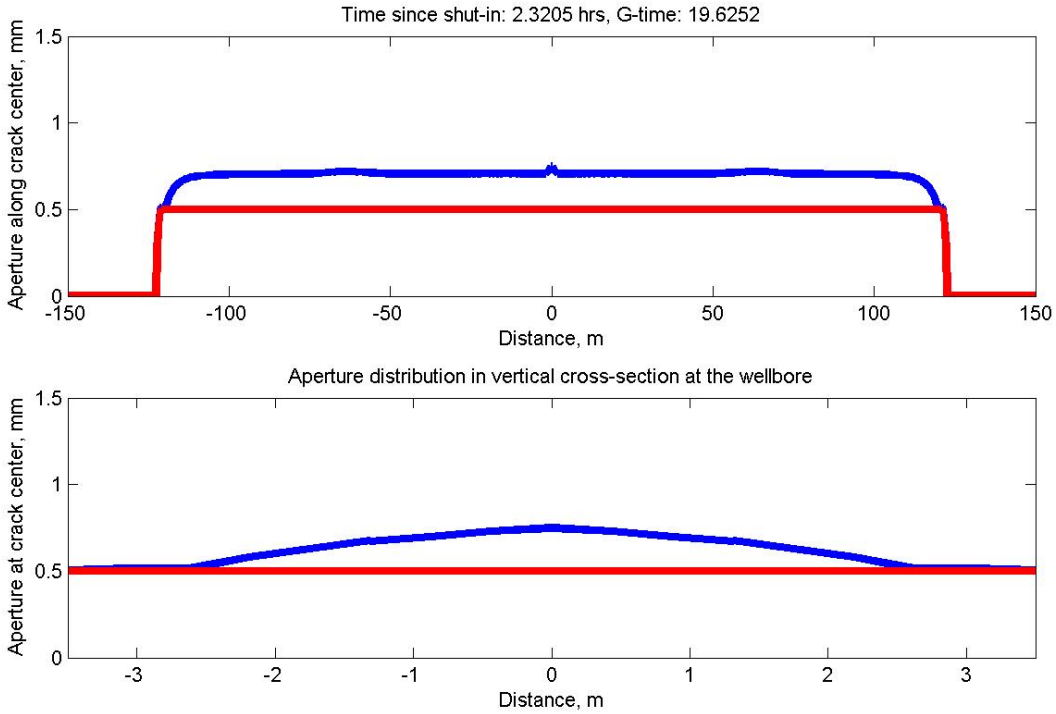

Figure 8: Distribution of aperture during Simulation G3 at 2.3205 hours after shut-in (19.6252 *G*-time). The upper figure shows aperture along the length of the fracture and the lower figure shows aperture along a vertical cross section at the center of the crack.

Figure 9 shows that at around 4 hours, the aperture had reached the residual aperture everywhere along the fracture. This was complete mechanical closure and coincided with the sharp increase seen in the derivative.

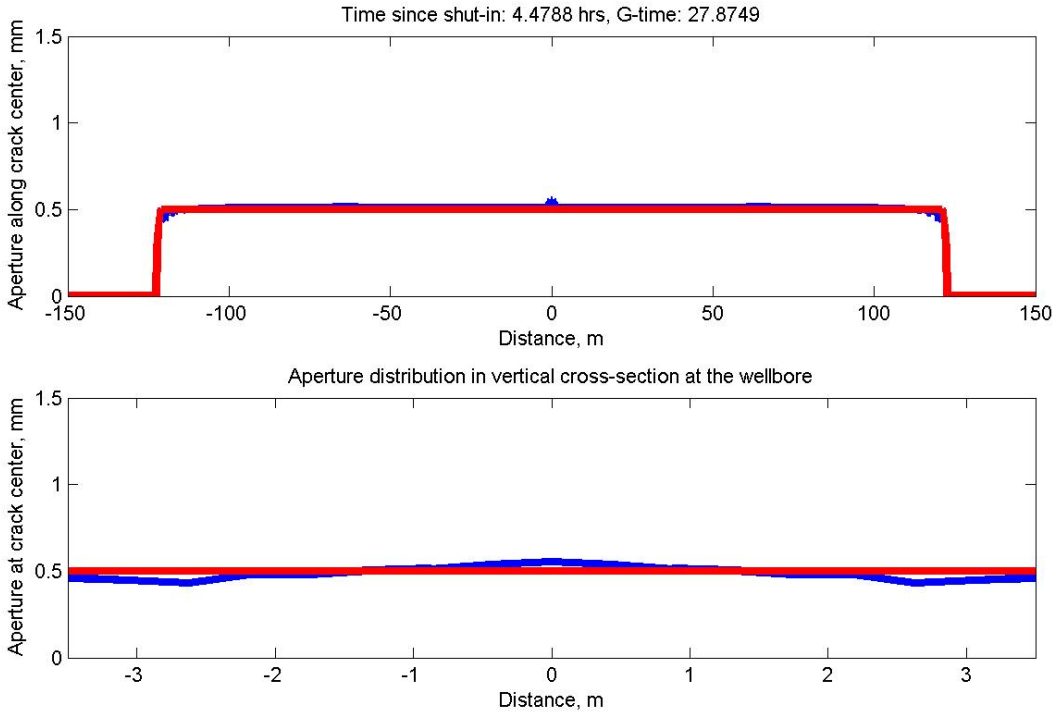

Figure 9: Distribution of aperture during Simulation G3 at 4.4788 hours after shut-in (27.8749 *G*-time). The upper figure shows aperture along the length of the fracture and the lower figure shows aperture along a vertical cross section at the center of the crack.

Even though fracture height recession occurred in this simulation (and occurs in all of the simulations with nonnegligible residual aperture), there is no ambiguity between its effect on the pressure transient and the effect of closure on the pressure transient. Figure 9 shows that the fracture closed fully by *G*-time of 28, coinciding with the time when $G \times dP/dG$ began to increase rapidly (Figure 6). The fracture height recession occurring prior to complete closure (seen by comparison between Figure 8 and Figure 9) over the period of around 20 *G*-time to 28 *G*-time caused a visible upward deflection of $G \times dP/dG$, but this deflection was slight compared to the much larger deflection that occurred after complete closure.

The true value of the minimum principal stress was 55.1 MPa. But the fluid pressure at the time of mechanical closure was slightly larger, about 57 MPa. This occurred because there is still some stress shadow on the fracture at closure as a result of the residual aperture. This stress shadow can be estimated by multiplying the residual aperture (500 microns) by the fracture stiffness due to elastic deformation of the formation, $S_{f,o}$ (calculated from Equation 19). This yields an estimate of 1.82 MPa, close to the overestimate that was observed.

3.1.3 Adding realism

In Simulation G3, several aspects of the simulation remained unrealistic. Wellbore storage was neglected, there was not near wellbore pressure loss, and there was still a rather sharp discontinuity in derivative with closure. In Simulation G4, these issues were resolved. Simulation G4 was similar to Simulation G3, but included wellbore storage and wellbore/near

wellbore pressure drop and used a much lower value of $\sigma_{n,ref}$, 5 MPa, to prevent a sharp increase in derivative with closure. From these values, we can calculate $S_{f,cont}$ to be 1.1 MPa/mm (Equation 21). This is less than the stiffness due to the elastic compliance of the surrounding formation, $S_{f,o}$ (3.64 MPa/mm). Thus when mechanical closure occurred in Simulation G4, the stiffness increased only fractionally, and a sharp discontinuity in pressure derivative was not seen.

The fracture formed after 36.6 seconds of injection, at a breakdown pressure of 61.15 MPa, before dropping down to a fracture propagation pressure around 60 MPa. The fracture propagation pressure was considerably higher than the ISIP because of the wellbore and near wellbore pressure drop.

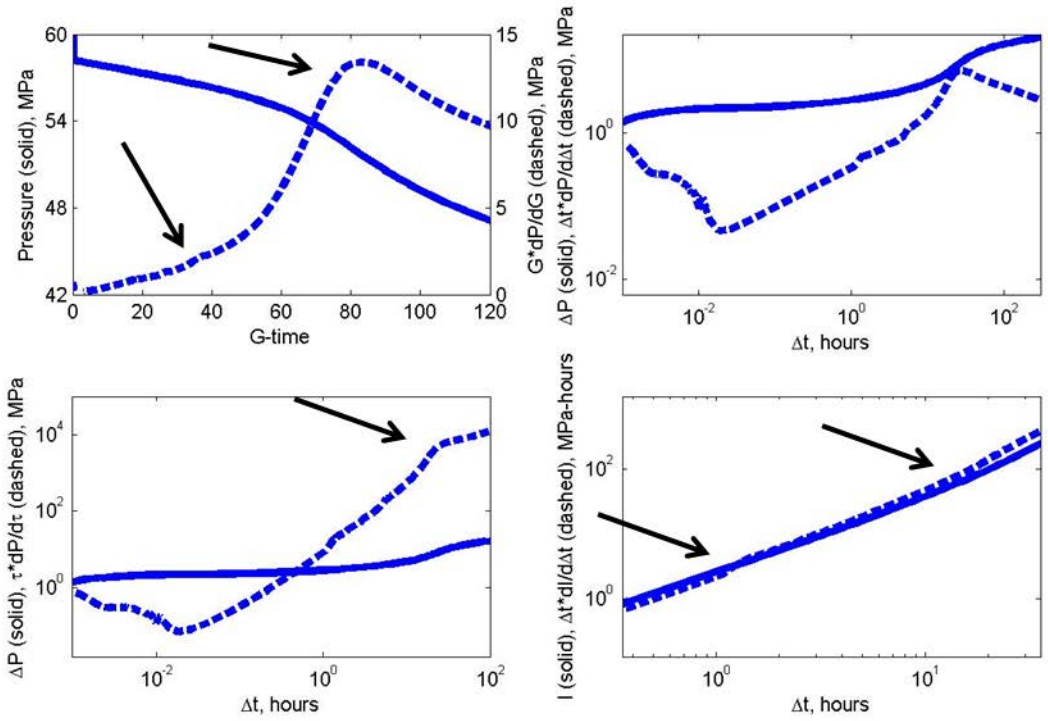

Figure 10: Results from Simulation G4. Upper left: *G*-function plot. Upper right: Bourdet plot with derivative with respect to time. Lower left: Bourdet plot with derivative with respect to superposition time. Lower right: Bourdet plot with integrated pressure (zoomed in).

The pressure transient in this simulation appears quite realistic and is similar to the match to field data described in Section 3.2. Using our proposed method, the closure pick is at *G*-time equal to 33, pressure of 56.7 MPa, and 4.3 hours after shut-in. The closure pick from the traditional method is at *G*-time equal to 77, pressure of 52.75 MPa, and 22 hours after shut-in.

The method of Mohamed et al. (2011) gives a similar closure pick as the traditional method. A small inflection in the Bourdet with superposition derivative curve is apparent at around 4 hours of shut-in (the time of closure according to our method), but it is almost imperceptible.

The Bourdet plot with integrated pressure gives a rather ambiguous pick for closure, with the first deflection of the curve at 1 hour (15.1 *G*-time), earlier than the interpretation from any other method. An inflection is also apparent at around 20 hours (73 *G*-time).

As in Simulation G3, fracture height recession occurred. However, this caused only the very slight concave upward behavior seen in the $G\times dP/dG$ curve from about G-time equal to 20 to G-time equal to 38. There is no ambiguity between this modest effect and the sharply increasing $G\times dP/dG$ curve from 38 G-time to 80 G-time, which would classically be interpreted as fracture height recession. The increasing $G\times dP/dG$ curve was caused solely by the increasing fracture stiffness after mechanical closure.

The wellbore and near wellbore pressure drop had the effect of causing a very rapid, brief period of pressure decrease immediately after shut-in.

3.1.4 Effect of maximum residual aperture

Several additional simulations were performed using the same settings as Simulation G4, but varying the maximum residual aperture, $E_{hf,res,max}$. These simulations used maximum residual aperture of 300 microns, 100 microns, and 50 microns. Figure 11 shows the results from these simulations, as well as the result from Simulation G4.

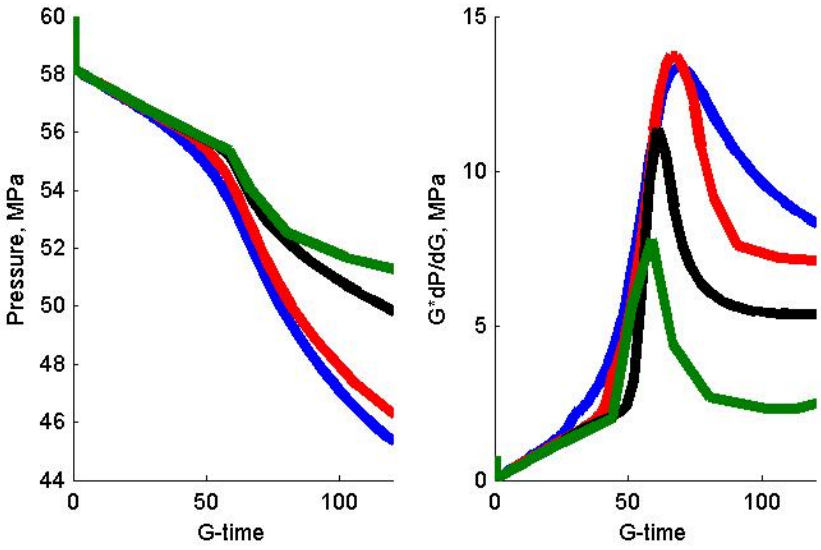

Figure 11: Reruns of Simulation G4 using different values for the maximum residual aperture. The left figure shows pressure versus G-time, and the right figure shows $G\times dP/dG$ versus G-time. The blue lines show the result from Simulation G4, with $E_{hf,res,max}$ equal to 500 microns. The red, black, and green lines show results with 300 microns, 100 microns, and 50 microns, respectively.

With smaller residual aperture, mechanical closure occurred later, at slightly lower pressure. This is because the stress shadow on the fracture due to the residual aperture at closure is smaller when the residual aperture is smaller. The increase in derivative became sharper with smaller residual aperture. Surprisingly, the overall amount of pressure decay decreased for lower values of $E_{hf,res,max}$. This was because aperture became so low after closure (especially because $\sigma_{n,ref}$ was only 5 MPa) that the fracture ceased to be of infinite conductivity at lower pressures and lower values of $E_{hf,res,max}$, which reduced the leakoff rate.

3.1.5 Fracture tip extension

Simulation G5 was performed with a much lower value of fracture toughness, 2 MPa-m$^{1/2}$. It was otherwise identical to Simulation G4. With this lower value of fracture toughness, a large amount of fracture tip extension occurred after shut-in. As in Simulation G4, the fracture formed after 36.6 seconds of injection, at a breakdown pressure of 61.15 MPa, before dropping down to a fracture propagation pressure around 60 MPa.

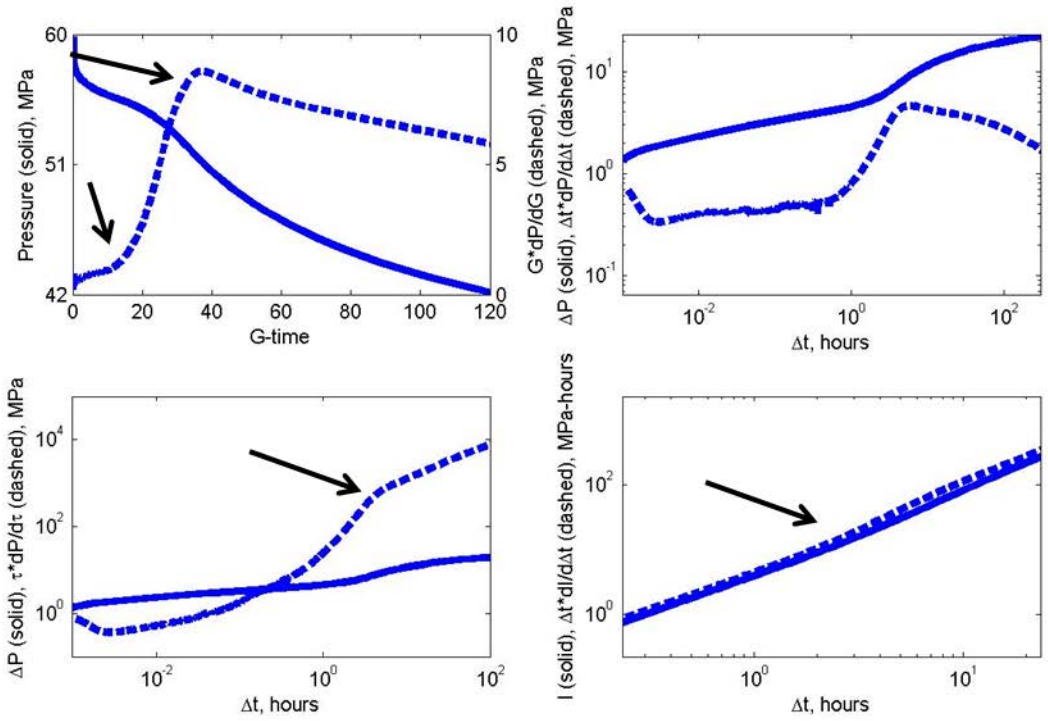

Figure 12: Results from Simulation G5. Upper left: *G*-function plot. Upper right: Bourdet plot with derivative with respect to time. Lower left: Bourdet plot with derivative with respect to superposition time. Lower right: Bourdet plot with integrated pressure (zoomed in).

The fracture tip extension is visible on the *G*-function plot. As described by Nolte (1991) and Barree and Mukherjee (1996), tip extension causes the $G \times dP/dG$ curve to increase sharply and then curve concave down. At shut-in, the fracture half-length was 110 m. However, after shut-in the fracture reached a half-length of 204 m. Fracture growth did not end until the fracture closed. The tip extension accelerated closure because it increased surface area and leakoff. Also, as the fracture grew, the average aperture along the fracture was forced to decrease in order to accommodate mass balance, causing aperture to reach the residual aperture sooner. The simulation was rerun with a residual aperture of 10 μm, and the fracture grew even longer, reaching a half-length of 280 m, and closure occurred later.

The high fracture length from this simulation may seem unrealistic for such a relatively modest volume of fluid pumped. We have performed simulations with multiple propagating fracture strands and found that the transient looks similar, but the overall fracture length is proportionally decreased, according to the number of fractures. Thus, the transient from a single fracture with a half-length of 200 m will be similar to the transient from multiple fracture strands, each with a length less than 200 m. Stress shadowing tends to cause only one or two fractures to propagate,

but wellbore and near wellbore pressure drop has the opposite effect, encouraging propagation of a larger number of fractures (which is the premise of limited-entry completion).

Investigation of the simulation results indicates that closure occurred at *G*-time equal to about 3.9 (0.1 hours) and a pressure of 56.5 MPa. Our proposed method would pick closure at a *G*-time of 12.7 (0.7 hours) and a pressure of 55.5 MPa. The traditional method would pick closure at *G*-time of 32.6 (4.2 hours) and pressure of 52.35 MPa. The Bourdet plot with superposition derivative method would pick closure at 3.2 hours (28.3 *G*-time) and a pressure of 53.3 MPa. The integrated pressure plot shows a deflection at about 2.5 hours (24.7 *G*-time) and a pressure of 54 MPa.

3.1.6 Higher permeability

Simulation G6 was performed with a permeability of 10^{-15} m^2 (~1 millidarcy), much higher than in the other simulations. As in Simulations G4 and G5, the fracture formed after 36.6 seconds of injection, at a breakdown pressure of 61.15 MPa, before dropping down to a fracture propagation pressure around 60 MPa.

Figure 13 shows that prior to mechanical closure, a straight line can be seen on the $G \times dP/dG$ plot, as expected. When mechanical closure occurred, at around 0.85 *G*-time (0.012 hrs), the rate of pressure drop decreased. This behavior was different from the previous cases, when closure caused the rate of pressure drop to increase. The different behavior can be understood by considering Equation 17, which shows that the rate of pressure decrease is equal to the product of fracture stiffness and leakoff rate. In a very low permeability formation, the fracture remains infinitely conductive (dimensionless fracture conductivity greater than 300) even after closure. But with higher permeability the dimensionless fracture conductivity rapidly drops below 300 after closure. As a result, the rate at which fluid can flow from the well (where fluid is stored due to wellbore storage) into the fracture is reduced by closure. If leakoff rate decreases enough to counteract the effect of increasing stiffness, the effect will be that closure decreases the rate of pressure decline.

With higher permeability, the fracture length is much shorter. Equation 17 shows that with lower fracture area, closure has a relatively smaller impact on the system "stiffness" and wellbore storage has a relatively larger effect. Thus, with higher permeability, closure has less effect on the overall stiffness, which lessens the tendency of closure to increase the derivative.

The linear flow period that corresponds to the straight line on the $G \times dP/dG$ curve can be seen from about 0.001 hrs to about 0.01 hrs on the Bourdet plot (upper right of Figure 13). After the linear flow period, the Bourdet derivative plot flattens out to a slope of approximately zero (with some gradual increase), corresponding to a radial flow period (which begins rapidly because of the higher permeability and lower fracture length), before finally reaching an impulse radial flow period with a negative one slope, starting at about one hour (*G*-time of 15). Comparison of the Bourdet plot with the *G*-function plot indicates that the $G \times dP/dG$ curve continued increasing after closure, though more slowly.

In the Bourdet plot with superposition derivative, the late time impulse radial appears as a flat line, as expected. The intermediate time, approximately radial, period shows a slope of 1.0,

which is expected because taking the derivative with respect to superposition time increases the log-log slope by one at shut-in times much greater than the period of injection (Section 1.2.2). Careful inspection of the Bourdet plot with respect to integrated pressure shows no indication of closure.

As in all previous cases, closure should be properly picked at the deviation from linearity of the $G\times dP/dG$ curve. However, in this relatively high permeability case, the slope of the $G\times dP/dG$ curve decreases after closure, rather than increasing.

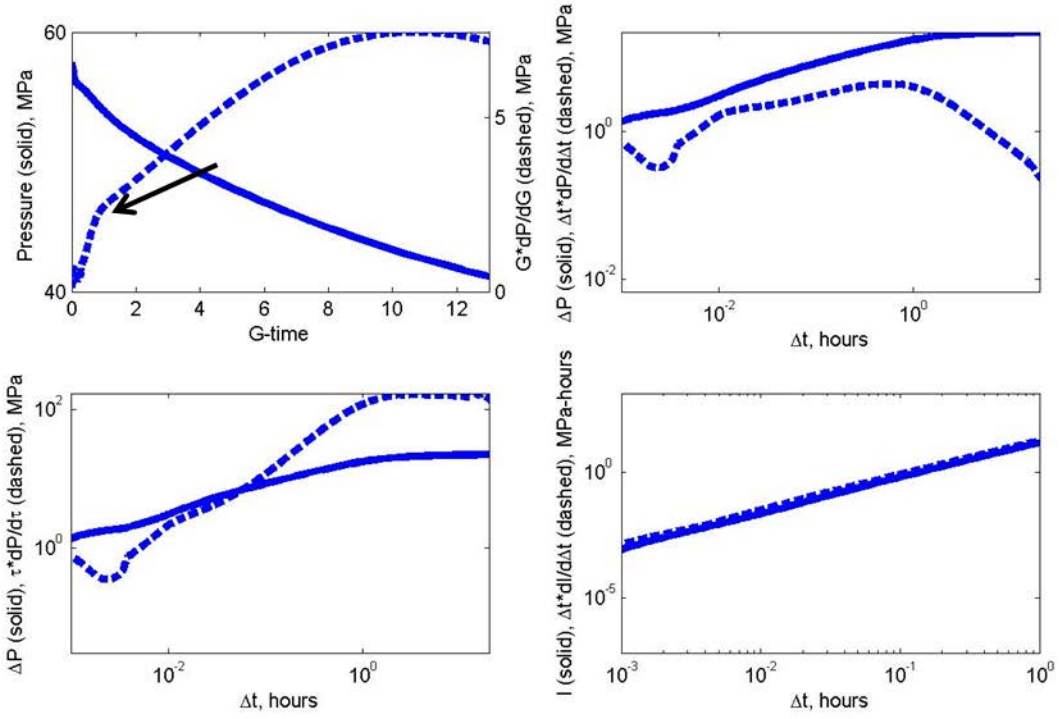

Figure 13: Results from Simulation G6. Upper left: *G*-function plot. Upper right: Bourdet plot with derivative with respect to time. Lower left: Bourdet plot with derivative with respect to superposition time. Lower right: Bourdet plot with integrated pressure.

3.2 Field DFIT #1

In this section, we review Field DFIT #1. This DFIT was previously shown on the left side of Figures 4 and 5 from Cramer and Nguyen (2013). The simulation we performed to match the data is called Simulation F1. The test was performed by injecting 1.83 m^3 (11.52 bbl) over 5.9 minutes into a vertical well perforated over a 5 m interval. The injection rate varied over time, as shown in Figure 16.

There are several reasons why this is an excellent example for assessing the ability of CFRAC to match DFIT transients.

(1) Cement integrity was excellent, as evidenced by the cement bond log, assuring adequate interzonal isolation throughout the injection and falloff periods.

(2) The test interval was mechanically strong (low clay content) and sufficiently thick (7 m) for establishing a dominant vertical hydraulic fracture. These mechanical characteristics are evinced by open-hole log signatures: neutron density, resistivity and sonic log responses (Figure 14).

(3) As evidenced in Figure 14, the stress contrast to higher-stress bounding rock layers is sufficient for containing a DFIT-scale fracture to the test interval.

(4) A conductive drilling induced tensile fracture was exhibited in the center of the test interval by an open-hole image log (Figure 15). This preexisting fracture facilitated non-complex, planar fracture initiation and propagation.

(5) The vertical orientation of the wellbore assures that the axial starter fracture will be in line with the plane normal to the minimum principal/horizontal stress, further reducing the potential for fracture complexity (Cramer and Nguyen, 2013).

(6) The pressure rollover event that was observed near the beginning of injection and at a relatively low bottomhole pressure is a strong indication that the preexisting fracture was reopened during the DFIT (Figure 16). Reopening of an existing fracture assures that the influence of wellbore hoop stress zone was mitigated or eliminated.

(7) The onset of the pressure rollover event, in which the pressure plot departs from the wellbore storage trend line (at 55.3 MPa), is in effect the fracture reopening pressure. This fracture reopening pressure should be slightly above the fracture closure pressure.

(8) There was a water hammer event at the end of injection, indicating that an excellent connection existed between the wellbore and primary, far-field fracture. This is assurance that there was no distortion of the shut-in pressure response due to near-wellbore fracture complexity or tortuousity.

(9) Borehole breakout analysis of adjacent intervals indicated the existence of a large difference between minimum and maximum horizontal stresses. Consequently, the probability of a primary hydraulic fracture interacting with and reopening crossed natural fractures is very low; transverse fracture storage is extremely unlikely.

(10) Permeability in the tested interval is very low, in the range of 50 - 150 nanodarcies. Consequently, dimensionless fracture conductivity should be very high following mechanical fracture closure, resulting in a stable fluid leak-off rate during closure. Thus, the change in fracture compliance/stiffness due to fracture closure should dominate the pressure falloff response when fracture closure occurs.

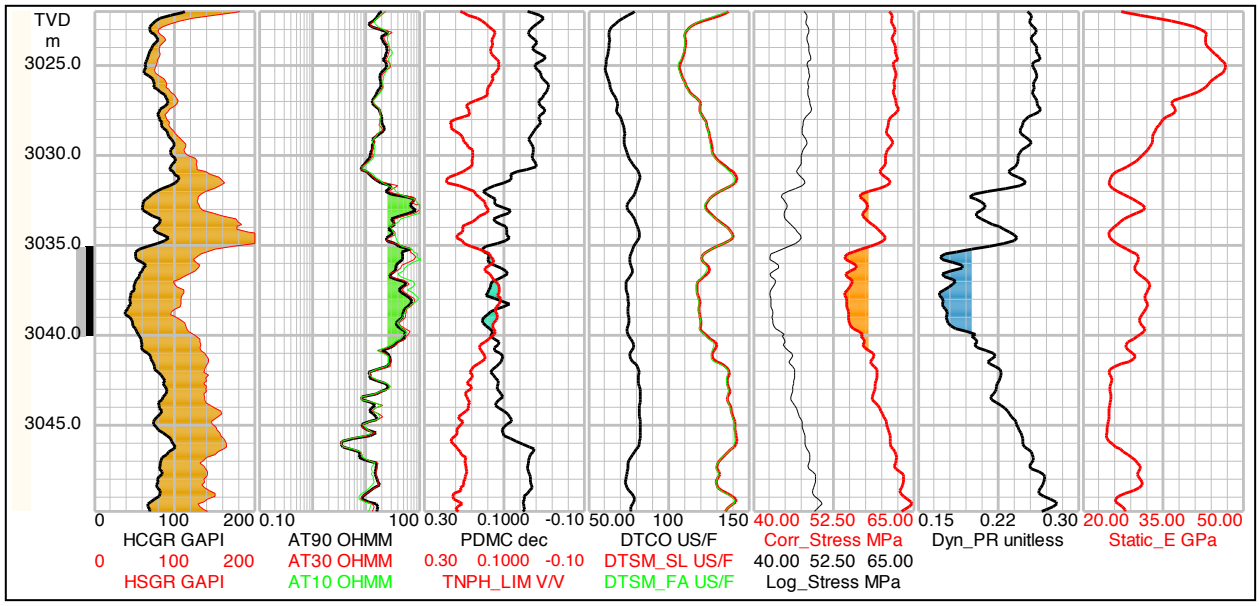

Figure 14: Open hole log data for Field DFIT #1

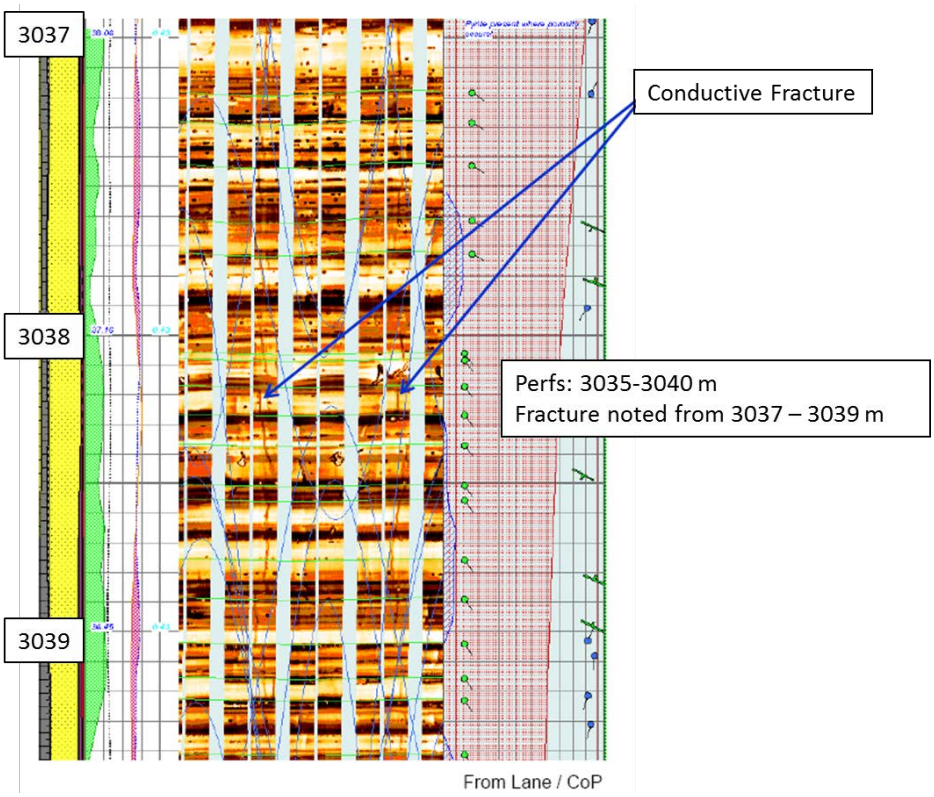

Figure 15: Wellbore imaging log for Field DFIT #1.

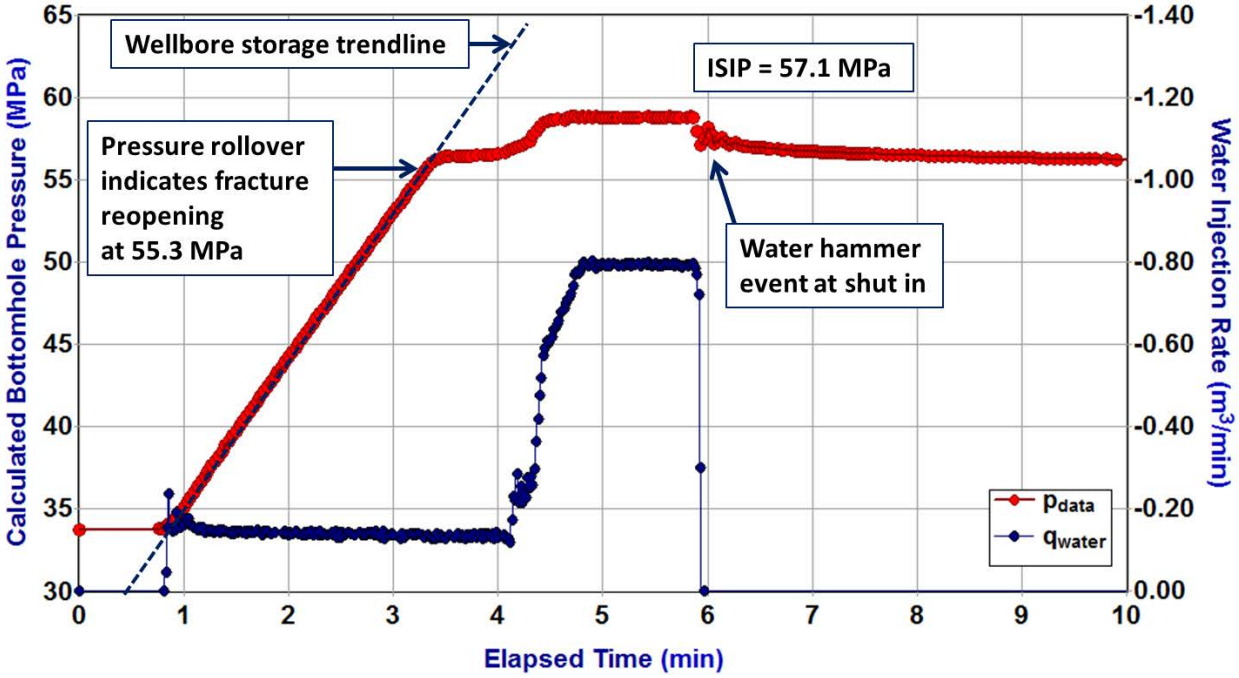

Figure 16: Pumping rate and calculated bottomhole pressure during injection and the start of the shut-in period for Field DFIT #1.

We generated a CFRAC simulation that very closely matched the field data. The simulation match was accomplished with a minimum principal stress equal to 54.3 MPa. This compares well to the fracture reopening pressure of 55.3 MPa, which was derived in analyzing Figure 16. The corresponding net pressure at the ISIP (57.1 MPa) is equal to 2.8 MPa, which is a reasonable value given the small injection volume and compatible with simulations performed with commercial planar fracture models.

Figure 17 shows the results. There was very brief period of rapid pressure drop at the start, as wellbore and near wellbore friction decreased. The $G \times dP/dG$ curve appears to be continuously concave upward during the shut-in period. However, a close examination of the data indicates that it forms a relatively flat straight period until about G-time of 7 (0.48 hours), when it begins to increase sharply. Thus, according to our proposed method of picking closure, the closure estimate should be at G-time of 7, for a pressure of 55.2 MPa. Plots of aperture versus position from the simulation results (similar to those shown in Section 3.1.2) confirm that closure occurred at G-time of 7 in the simulation. Fracture closure occurred at a pressure about 0.9 MPa greater than σ_{hmin} because of the stress shadow caused by the residual aperture.

The traditional method would yield an estimate of closure pressure around G-time of 36 (about 9.4 hours), which is a pressure around 49.3 MPa. The net pressure corresponding to this estimate is 7.8 MPa, which is unrealistically high given the small injection volume. The Mohamed et al. (2011) method of picking closure would identify closure at about 8 hours (G-time of 33.2), for a pressure of about 50 MPa. There is a slight deviation in the Bourdet plot with integrated pressure curve at around 4 hours (G-time of 23) and at pressure of 52.5 MPa.

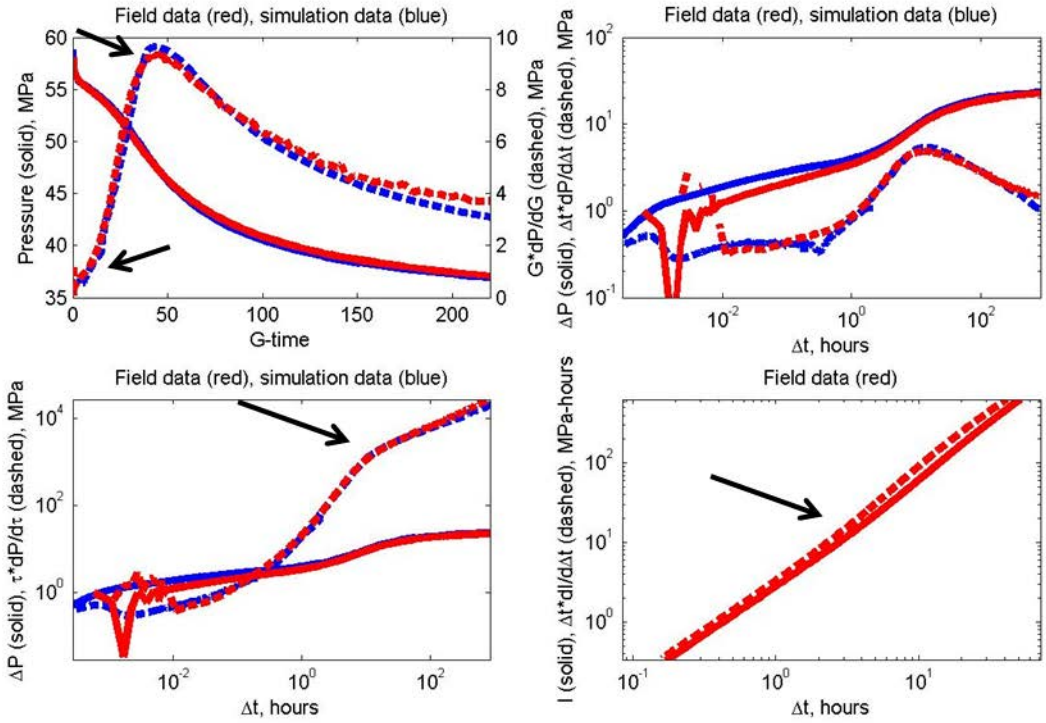

Figure 17: Comparison of field data and simulation match for field DFIT #1. Upper left: *G*-function plot. Upper right: Bourdet plot with derivative with respect to time. Lower left: Bourdet plot with derivative with respect to superposition time. Lower right: Bourdet plot with integrated pressure (zoomed in).

3.3 Field DFIT #2

In this section, we review Field DFIT #2. This DFIT was previously shown in Figure 52 of Cramer and Nguyen (2013). The simulation we performed to match the data is called Simulation F2. This is the most challenging example presented in this paper, and our interpretation is the most uncertain.

Field DFIT #2 was performed from a single perforation cluster in a horizontal wellbore. A volume of 1.08 m^3 (6.8 bbl) of fluid was injected over 8.25 minutes. The leakoff point was reached after 3.3 minutes of injection at 83.8 MPa. Figure 18 shows a plot of fluid pressure versus volume injected. Figure 19 shows plots of the field data and a CFRAC simulation match to the data.

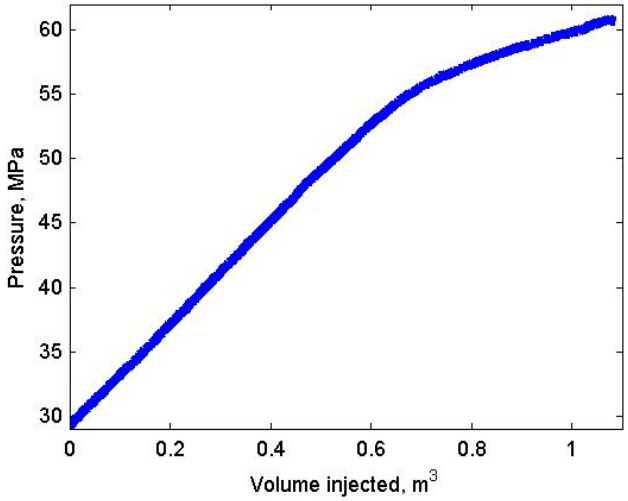

Figure 18: Field data from Field DFIT #2. Plot shows pressure versus volume injected during pumping.

Figure 18 shows that shut-in was performed before a stable fracture propagation pressure was reached. As can be inferred from the figure, at the time of shut-in, most of the injected fluid remained stored in the wellbore. The fluid continued to gradually leak out into the fracture during shut-in, significantly impacting the pressure transient.

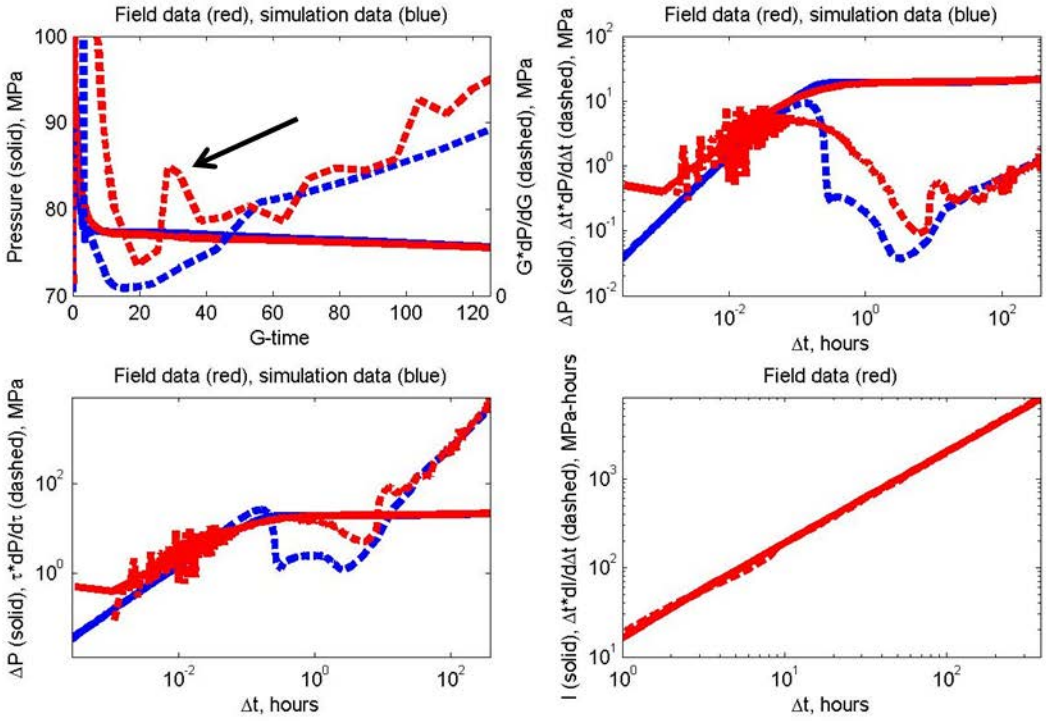

Figure 19: Comparison of field data and simulation match for Field DFIT #2. Upper left: *G*-function plot. Upper right: Bourdet plot with derivative with respect to time. Lower left: Bourdet

plot with derivative with respect to superposition time. Lower right: Bourdet plot with integrated pressure (zoomed in).

The simulation did a reasonable job of matching the field data, though the match is imperfect at intermediate time. Initially, there was a rapid drop in pressure as the wellbore and near wellbore pressure drop was dissipated and fracture tip extension occurred. The early drop in pressure had equal magnitude in the data and in the simulation, but in the data, it was spread over a significantly longer period of time. Periods of rapidly dropping pressure after shut-in are common, but the period lasted unusually long in this transient, an indication of near wellbore complexity, with the issue exacerbated by the small injection volume.

Around G-time equal to 12, the pressure in the field data flattened out, reaching the conventional "pre-closure" period. According to our proposed method, closure would be picked at G-time equal to 26 (9.8 hours) and 77 MPa. At this point, $G \times \mathrm{d}P/\mathrm{d}G$ spiked and then started increasing steadily. In the simulated transient, closure would be picked even earlier (though at an almost identical pressure), around G-time of 15. The simulated fluid pressure at that time was 77.3 MPa, very close to the minimum principal stress used in our simulation match to the data. Careful investigation of plots of aperture from the simulation results (as shown in Section 3.1.2) indicates that closure occurred in the simulation from about 0.5 to 2 hours (G-time of 4.8-11), corresponding to a pressure range of 77.6 MPa to 77.3 MPa.

While we were able to approximately match the data with a simulation in which closure occurred during the transient, we cannot rule out the alternative interpretation that closure did not occur during the transient. The pressure decay was exceptionally slow, and as a result it was necessary to use an exceptionally low permeability, 3×10^{-22} m^2 (~0.3 nanodarcies). As an alternative, we attempted to match the data with simulations where closure did not occur during the transient. We increased the fracture toughness to shorten the fracture, which delayed closure and reduced the rate of leakoff and pressure decay. To compensate for the reduced rate of pressure decay due to the shorter fracture, we increased the permeability. These simulations were able to match part of the data, but always predicted that closure would occur prior to the end of the transient, which lasted for 293 hours of shut-in time. Therefore, we were unable to find a match to the data in which closure did not occur before the end of the transient.

Possibly, such low leakoff rates from the fracture could be explained by multiphase flow effects as water leaks off into the hydrocarbon saturated shale matrix. On the other hand, it is also possible that this transient, which exhibited strong evidence of near wellbore fracture network complexity, cannot be adequately described by a model that assumes only a single planar fracture propagating away from the wellbore. For example, perhaps near wellbore complexity caused a pinchoff of the hydraulic connection between the well and the far-field fracture. This could hydraulically isolate the wellbore from the far-field fracture and have unpredictable effects on the observed pressure transient.

If closure did occur during the transient, then linear flow (scaling of ΔP with the square root of time), not impulse linear flow (scaling of ΔP with the inverse of the square root of time) would have occurred after closure, at odds with the assumptions made by Mohamed et al. (2011) and Barree et al. (2007). Mohamed et al. (2011) proposes picking closure at the end of the 3/2 slope on a Bourdet plot with superposition time derivative, which is equivalent to the end of the 1/2 slope on a standard Bourdet plot. In this simulation, the 3/2 slope existed for long after closure

occurred. Barree et al. (2007) stated that closure has not occurred if the $G \times dP/dG$ curve is continuing upward, but in our simulation result, that was not the case.

Linear flow was possible after shut-in because of the relatively high wellbore storage and very low matrix permeability. As shown in Appendix B, the timing of the transition between linear flow and impulse linear flow is dependent on the square of the effective fracture compliance (which we define as the reciprocal of fracture stiffness plus the fracture area divided by the wellbore storage coefficient) divided by the matrix permeability. Fracture closure decreases the effective fracture compliance, which accelerates the onset of impulse linear, but it is still possible for standard linear flow (rather than impulse linear) to continue after closure. With sufficient shut-in time, the transient would have eventually reached impulse linear flow and reached a 0.5 slope on the Bourdet with superposition derivative plot (-0.5 slope on the standard Bourdet plot).

This field example shows the importance of pumping a sufficiently large volume of water after breakdown.

3.4 Field DFIT #3

In this section, we review Field DFIT #3. This DFIT was previously shown on the left side of Figure 53 from Cramer and Nguyen (2013). The simulation we performed to match the data is called Simulation F3.

Field DFIT #3 was performed from a vertical wellbore. A volume of 2.86 m^3 (18.0 bbl) of fluid was injected over 9.9 minutes. In the data, the leakoff point occurred after 3.95 minutes of injection at 86.5 MPa. Figure 20 shows the field data and the results of a CFRAC simulation designed to match the data. The minimum principal stress assumed in the simulation match was 83.5 MPa. The difference between the final injection pressure and the ISIP was (depending on choice of ISIP) from 2-4 MPa, roughly the pressure difference between the leakoff point and the minimum principal stress from our simulation match, which corroborates our estimate of σ_{hmin}.

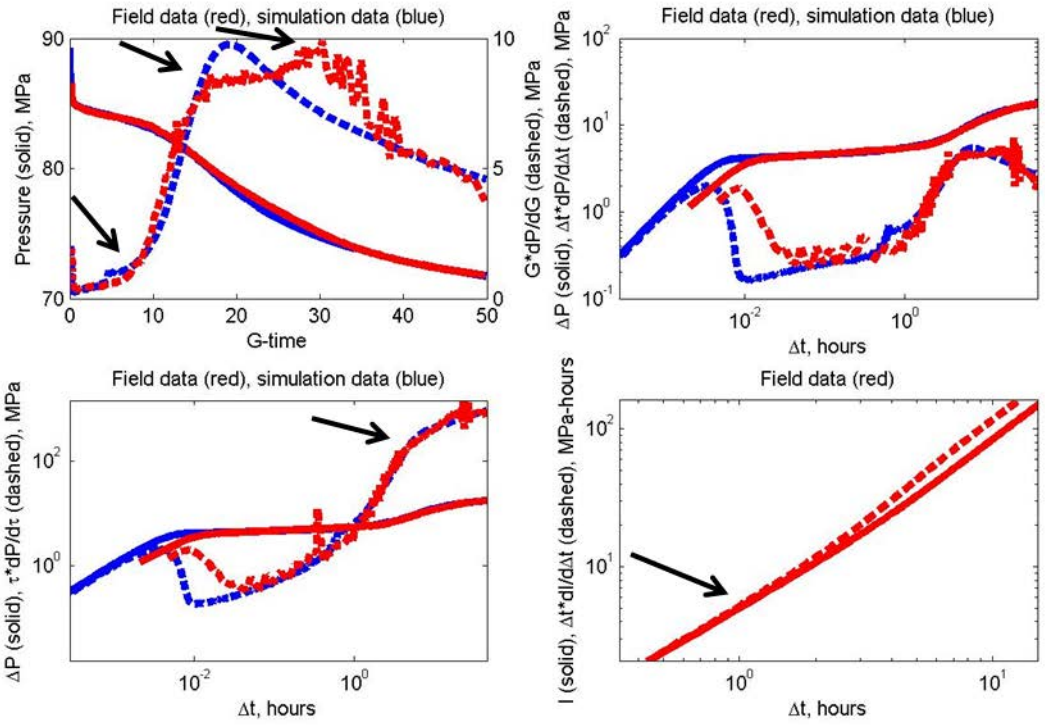

Figure 20: Comparison of field data and simulation match for Field DFIT #3. Upper left: *G*-function plot. Upper right: Bourdet plot with derivative with respect to time. Lower left: Bourdet plot with derivative with respect to superposition time. Lower right: Bourdet plot with integrated pressure (zoomed in).

The *G*-function plot shows a very brief initial period of pressure decrease, much briefer than in Field DFIT #2. Then the transient settles into a period of roughly linear, low slope $G \times dP/dG$ before showing a sharp, concave upward increase. In the field data, the $G \times dP/dG$ curve does not smoothly peak and decline, but rather increases sharply, enters a period of more gradual increase, and then finally begins to decline. The extended, almost double, peak in the $G \times dP/dG$ curve was probably caused by some form of complexity in the fracture network. Because the CFRAC simulation involved only a single fracture, it was unable to match that effect.

According to the traditional method, closure might be picked near the first peak in $G \times dP/dG$, at *G*-time of 15.6, corresponding to 5.0 hours and a pressure of 80.6 MPa. Alternatively, closure might be picked at *G*-time around 30.3, corresponding to a time of 17.1 hours and a pressure of 74.9 MPa. A pick based on our proposed method would be at a *G*-time of about 6.5, corresponding to a time of 1.08 hours and a pressure of 83.8 MPa (close to the value of σ_{hmin} from the simulation match).

In the Bourdet plot with superposition derivative, the 1.5 slope ends at about 4 hours, corresponding to a pressure of 81.7 MPa. In the Bourdet plot with integrated pressure, separation is apparent at about 1 hour (*G*-time of 6.2), a pressure of 83.8 MPa. In this case, the Bourdet plot with integrated pressure gives a closure pick very close to our proposed method.

3.5 The GRI/DOE M-Site Tests

The GRI/DOE M-Site project involved a series of hydraulic fracturing injections into two intervals - the "B-sand" and the "C-sand." In this section, we consider the tests in the B-sand. The B-sand consisted of a complex sequence of sandstone, mudstone, siltstone, and shale. The site was unusually well-instrumented, involving a microseismic array and downhole tiltmeters in an offset well (Branagan et al., 1996a). The tiltmeters provide an independent estimate of the minimum principal stress. In the B-sand, seven different injection tests were performed, some involving clear water, others involving gelled or cross-linked fluid, and one involving proppant. Pump-in fluid volume during these tests ranged from 3.0-95 m^3 (19 to 600 bbl). Pressure measurements were taken for an extended time after shut-in for two of the tests: the initial breakdown injection, which involved 3.0 m^3 (19 bbl) of cross-linked gel pumped at 13.25 l/s (5 barrels/min), and injection 6B, which involved 63.6 m^3 (400 bbl) of linear gel pumped at 58.3 l/s (22 barrels/min). The matrix permeability was estimated to be 0.1 mD (~10^{-16} m^2), significantly higher than the field cases previously considered in this paper.

Figure 21 shows the result from the initial breakdown injection test. Breakdown of the formation occurred 2.7 minutes prior to shut-in at 30.77 MPa before dropping to a fracture propagation pressure of about 27 MPa.

The 6B injection shut-in transient was unusual (showing no clear indication of closure at any pressure), was the sixth injection into the interval, and used a much larger volume than is typically used in a DFIT. Therefore, the results from that test are not presented.

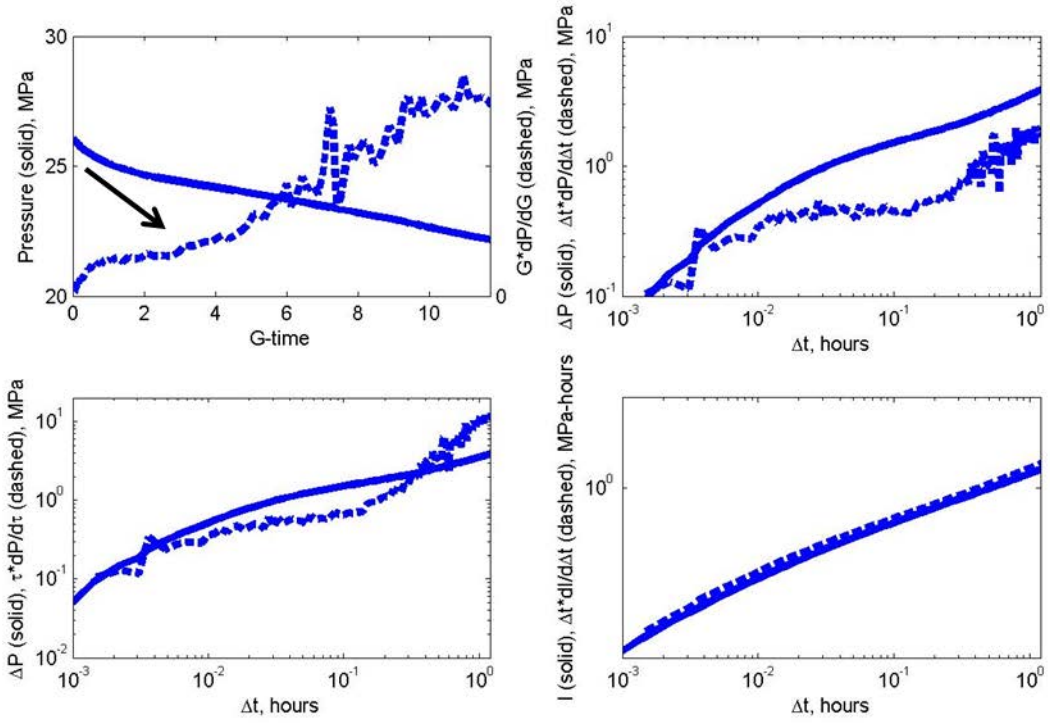

Figure 21: Field data from the M-site, B-sand breakdown injection. Upper left: *G*-function plot. Upper right: Bourdet plot with derivative with respect to time. Lower left: Bourdet plot with derivative with respect to superposition time. Lower right: Bourdet plot with integrated pressure.

The *G*-function plot shows a period of fracture tip extension at early time, during roughly the first 1.0 *G*-time. Afterwards, the $G \times dP/dG$ curve flattens out before beginning to increase

sharply after about G-time of 3.5 (0.16 hours). According to our proposed method of picking closure, this increase in the $G \times dP/dG$ curve represents closure, and so the minimum principal stress should be picked from the pressure at G-time of 3.5, 24.3 MPa. This is seen in the Bourdet plot near the beginning of the 1/2 slope. In the Bourdet with superposition time plot, this is the time at which the 1.5 slope begins. In the Bourdet with integrated pressure plot, there is no apparent deflection that indicates closure, even if the plot is zoomed in.

Using the traditional method of G-function analysis and the Mohamed et al. (2011) method, it might be argued that closure is happening at the end of the dataset, around 0.85 hour of shut-in (G-time of 9.5), corresponding to a pressure of 22.75 MPa. However, it is possible that if the transient had lasted longer, a later pick of closure could have been made.

Figure 22 shows the normalized tiltmeter response plotted against wellbore pressure during injection 2B, the test immediately after the breakdown test shown in Figure 21. A smoothed version of this figure was shown in Figure 9A-4 of Economides and Nolte (2000). Each tiltmeter response is normalized by dividing by the maximum tilt measured at that instrument during the test. The tiltmeters demonstrate that the fracture began opening at about 23.9 MPa, very close to the closure pressure that we estimated from the shut-in transient after the breakdown injection (which immediately preceded the 2B injection). At 23.9 MPa, the derivative of tilt with respect to pressure became much greater, indicating an abrupt drop in fracture stiffness at that pressure, indicating reopening.

The plot shows only the data during injection, not shut-in. The shut-in tiltmeter response is much smoother and shows a more gradual relationship between tilt and wellbore pressure. This difference is due to the contribution to the tiltmeter response from the poroelastic effect of the fluid leaked off into the formation. During injection, the amount of leakoff was relatively minimal, which is why the tiltmeter response during injection (reopening) is more appropriate for estimating the minimum principal stress.

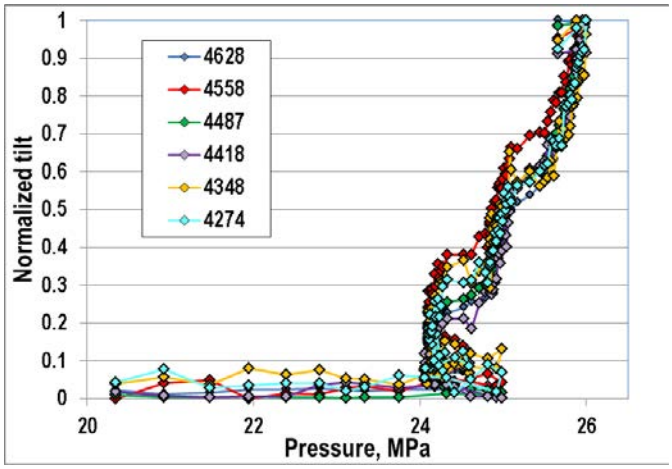

Figure 22: Normalized tiltmeter data from injection B2 from the GRI/DOE M-site. Data courtesy of Norm Warpinski.

Branagan et al. (1996a) reported that the tiltmeters detected substantial residual deformation (20% of the maximum deflection) many weeks after the first four injections into the B-sand. The duration of shut-in was sufficient such that the fluid pressure perturbation had dissipated into the surrounding formation, and so the observed residual deformations were unlikely to have been

caused by poroelastic effects. Instead, Branagan et al. (1996a) interpreted these results as suggesting that the fractures retained significant residual aperture after closure. Their finding supports a key premise of our modeling approach: that hydraulic fracture residual aperture is significant and has a substantial effect on pressure transients from diagnostic fracture injection tests.

3.6 Non-uniqueness in simulation results

The simulation matches to the field data are subject to non-uniqueness. Lower shear modulus, higher fracture toughness, and greater fracture height (or radial geometry) all result in lower fracture surface area, which can be compensated by using a higher permeability or lower fluid viscosity. The selection of fluid viscosity is complicated because in most cases clear water is being injected into a gas or oil saturated formation. Leakoff will be affected by multiphase effects such as relative permeability and capillary pressure, and the injection fluid has a different viscosity and compressibility than the reservoir fluid. In the simulations in this paper, we have not even made an attempt to choose a realistic viscosity and have merely set the fluid viscosity to 1 cp. Adjustments to viscosity require proportional adjustments to the permeability in order to achieve a simulation match.

Because of this non-uniqueness, many of the values used in the simulation matches should not be interpreted as being actual estimates for those parameters in the formation. However, there are certain features of the transients that allow unique estimation of formation parameters. For example, in all cases, the wellbore storage coefficient can be estimated with high confidence from the slope of a plot of pressure versus volume injected prior to the leakoff point or breakdown pressure. The shear moduli in the simulation matches were chosen based on estimates available from core or geophysical logs.

We found that the estimates for closure pressure based on the simulations matches were unique. In every case, closure caused the $G\times \mathrm{d}P/\mathrm{d}G$ curve to deflect upward (except the high permeability case, when it deflected downward). Therefore, the location of the deflection in the $G\times \mathrm{d}P/\mathrm{d}G$ curve can be taken as a unique estimate for the closure pressure. Because the residual aperture creates a stress shadow, the closure pressure estimate could be up to 1-2 MPa greater than the actual value of σ_{hmin} (depending on the magnitude of the residual aperture and the geometry of the fracture), which creates some uncertainty.

Processes such as fracture height recession and opening/closure of transverse fractures have been used in the literature to explain challenging data. While these processes may sometimes occur in field data, our results suggest that with a simulation model that properly sets up and solves the problem, including the effect of residual aperture and wellbore storage, many or most field cases can be explained with a simple planar fracture model that does not include these processes. In the future, extensions of our model could be used to investigate more complex behaviors such as pressure dependent leakoff.

As we showed, field data usually does not show an extremely sharp increase in derivative at closure. For this observation to hold true, the increase in joint stiffness due to closure cannot be excessively large (discussed in Section 3.1.1.1). For the cases we considered, this suggests the residual aperture should be modeled as being on the order of at least several hundred microns.

Calculations of fracture length are highly non-unique because of uncertainty about height, geometry, and the possibility of multiple fracture strands. Many in-situ observations of hydraulic fracture geometry that have found multiple fracture strands (Warpinski and Teufel, 1987; Warpinski, 1993; Branagan et al., 1996b; Mahrer, 1999). For example, at the GRI/DOE M-site project discussed in Section 3.5, microseismicity formed into a relatively narrow planar region. But when a well was cored across the fracture, 11 fractures were intersected in a 2.6 foot wide interval at a distance of 126 feet from the injection well (Branagan et al., 1996b).

We performed simulations in which multiple fractures were assumed to be propagating away from the wellbore at a spacing of three meter. Because the Vinsome and Westerveld (1980) method for calculating leakoff does not account for neighboring fractures, we used a 2D version of CFRAC in which leakoff is handled fully numerically and can account for interference between fractures (McClure, 2014b). The simulations showed that if multiple strands propagate, this has only a modest effect on the shape of the transient, but proportionally reduces the length of the strands. A simulation match with one fracture of half-length of 200 feet is equivalent to a simulation with four fractures with average half-length of 50 feet. Stress shadowing tends to prevent propagation of multiple strands, but perforation pressure drop resists this effect, distributing flow across multiple fractures.

Because the fractures may be non-planar, branching, and have multiple strands, it is uncertain whether pre-closure fracture stiffness can be estimated from analytical solutions such as Sneddon (1946) that assume simple fracture geometry.

The net pressures implied by the traditional method of *G*-function interpretation and the Mohamed et al. (2011) method are much higher than the values derived from our proposed method. Matching these very high net pressures would require very high assumed values of fracture toughness or poorly constrained adjustments for a fluid-lag zone or inelastic deformation ahead of the crack tip (Jeffrey, 1989; Yew and Liu, 1993; Mack and Warpinski, 2000). This is not impossible, but in the context of the results from this study, the more parsimonious explanation is that net pressure is overestimated due to the method of DFIT interpretation. The lower net pressures implied by our estimates for σ_{hmin} can be matched with values of fracture toughness consistent with laboratory measured values.

3.7 Validation with pump-in/flow-back tests

The example in Section 3.5 gives independent validation of our proposed method for estimating the minimum principal stress. But in practice, downhole tiltmeters arrays will seldom be available. Pump-in/flow-back tests are an alternative method for estimating the minimum principal stress and can be performed at relatively minimal cost (Soliman and Daneshy, 1991; Plahn et al., 1997; Raaen and Brudy, 2001; Raaen et al., 2001). Raaen et al. (2001) showed how the closure pressure can be picked from the inflection point in a plot of pressure versus flow-back volume. If operators are interested in testing methods for picking closure pressure, they could perform a DFIT, and then subsequently perform a pump-in/flow-back test. The results from the pump-in/flow-back test could be compared to the results from the DFIT test.

4. Conclusions

1. Using a hydraulic fracturing simulator that includes the effect of residual fracture aperture, we showed that simulations of diagnostic fracture injection tests (DFITs) can be performed that closely match field data, including the pre-closure, closure, and post-closure periods.

2. In Appendix A, a general equation is derived for pressure transient behavior during a DFIT. This equation is more general than expressions used previously by others in the literature and can be used to explain the results of the simulations and field cases provided in this paper.

3. The results suggest that the traditional method for identifying closure from *G*-function plots advocated by Barree et al. (2007) and others tends to underestimate the minimum principal stress in low permeability formations. The traditional method neglects the fact that leakoff can continue to occur from the part of the fracture that is mechanically closed and that closure causes an increase in the pressure derivative due to increasing fracture stiffness. In high permeability formations, closure can cause a decrease in the pressure derivative by decreasing the rate of fluid leakoff.

4. The method proposed by Mohamed et al. (2011) for picking closure from a Bourdet plot with superposition time derivative tends to give results similar to the traditional method of picking closure from *G*-function plots.

5. The method Craig and Blasingame (2006) proposed for identifying closure from a Bourdet plot with integrated pressure is based on picking closure from a change in storage and thus has the potential to identify the correct closure pressure. However, the deflection on the plot is often too small or ambiguous to be used to make the correct pick.

6. Our results suggest closure can best be picked using the original concept of picking closure from a *G*-function plot (Castillo, 1987) or a square root of time plot (Zoback, 2007). This concept is to identify the departure from linearity on the plot of pressure versus *G*-time or the square root of time (after the very early time period after shut-in when dissipating wellbore and near wellbore friction causes the pressure to drop rapidly). Identification of this departure from linearity can be assisted by the $G \times \mathrm{d}P/\mathrm{d}G$ curve. In low permeability formations, the $G \times \mathrm{d}P/\mathrm{d}G$ curve should deflect upward at closure. We did not exhaustively consider interpretation in high permeability formations, but in the high permeability case we considered, the $G \times \mathrm{d}P/\mathrm{d}G$ curve deflected downward when closure occurred because closure reduced the rate of leakoff.

7. The residual fracture aperture upon closure can cause a stress shadow of up to 1-2 MPa. As a result, the closure pressure can be as much as 1-2 MPa above the value of the minimum principal stress.

8. In a fracture injection test from the GRI/DOE M-site project, the closure pick was independently estimated from downhole tiltmeters. The results show that our proposed method provides the best pick for closure pressure.

9. It is possible for a formation linear flow period (1/2 slope on a conventional Bourdet plot, 3/2 slope on a Bourdet plot with superposition time) to occur after closure. This contradicts the methods of closure identification proposed by Mohamed et al. (2011) and Barree et al. (2007).

10. In our simulation matches to field data, there was considerable non-uniqueness with respect to parameters such as fracture toughness and permeability. However, the upward deflection of the $G \times \mathrm{d}P/\mathrm{d}G$ curve always occurred at the closure pressure. This indicates that the closure pressure can be uniquely determined from the shut-in transient.

11. Some DFIT transients are too complex to be interpreted using the simple method for picking closure provided in point #5 above. In these cases, numerical modeling could be used to investigate the causes of these more complex transients. But for numerical models to give valid physical insights, it is critical for them to be properly set up. They must perform discrete fracture simulation and correctly specify governing equations, constitutive equations, and boundary conditions. They must account for residual aperture after closure, wellbore storage, perforation and near wellbore frictional pressure drop, and use a leakoff model that accounts for the changing pressure in the fracture over time.

Acknowledgements:

The financial support provided by the Fracturing and Sand Control JIP at The University of Texas at Austin is gratefully acknowledged. The authors would like to thank Norm Warpinski for supplying data from the GRI/DOE M-site project used in the paper and Priscila Ribeiro and Bertrand Rohmer for their useful comments. Thank you to our friends and colleagues who have encouraged us in pursuing this research.

List of variables:

A: fracture area (m^2)

a: element half-length (m)

C_{ac}: after-closure storage coefficient (m^3/MPa)

C_f: fracture compliance (m/MPa)

$C_{f,eff}$: effective fracture compliance (m/MPa)

C_{fD}: dimensionless fracture conductivity (unitless)

C_{nw}: constant for wellbore and near wellbore pressure drop (MPa/(m^3/s)^2)

C_w: wellbore storage coefficient (m^3/MPa)

C_t: total storage coefficient for fracture and wellbore system (m^3/MPa)

c_f: fluid compressibility (MPa^{-1})

c_ϕ: porosity compressibility (MPa^{-1})

E: void aperture (m)

E_0: residual fracture aperture (m)

$E_{hf,max,resid}$: maximum residual aperture (m)

E_{open}: mechanical fracture opening (m)

e: hydraulic aperture (m)

G: G-time (unitless)

G_m: shear modulus (MPa)

h_f: fracture height (m)

I: integrated pressure (MPa-s)

K_I: stress intensity factor (MPa-$m^{1/2}$)

K_{Ic}: fracture toughness (MPa-$m^{1/2}$)

k: permeability (m^2)

L_f: fracture half-length (m)

m: mass of fluid in the wellbore and fracture (kg)

P: fluid pressure (MPa)

P_0: reference pressure used to calculate fluid density (MPa)

P_D: dimensionless pressure (unitless)

P_{DE}: dimensionless pressure at early time (unitless)

P_{DL}: dimensionless pressure at late time (unitless)

$P_{f,init}$: initial fluid pressure in the fracture (MPa)

P_{init}: initial fluid pressure (MPa)

Q: volumetric flow rate (m^3/s)

Q_{cum}: cumulative volumetric leakoff (m^3)

Q_{slug}: volume of injected fluid (m^3)

q_{flux}: mass flux (kg/(m^2-s))

q_{inj}: volumetric surface injection rate (m^3/s)

$q_{m,inj}$: surface mass injection rate (kg/s)

$q_{leakoff}$: total volumetric leakoff rate across entire fracture (m^3/s)

$q_{m,leakoff}$: total mass leakoff rate across entire fracture (kg/s)

$q_{m,leakoff,a}$: mass leakoff rate per area (kg/(m^2-s))

R_f: fracture radius (m)

S: volume of fluid stored (m^3)

S_f: fracture stiffness (MPa/m)

$S_{f,c}$: stiffness of a closed fracture (MPa/m)

$S_{f,cont}$: contribution to stiffness of a closed fracture from contact stress (MPa/m)

$S_{f,o}$: stiffness of open fracture, or equivalently, contribution to stiffness of a closed fracture from the deformation of the surrounding formation (MPa/m)

$S_{f,PKN}$: stiffness of an open PKN fracture (MPa/m)

$S_{f,r}$: stiffness of an open radial fracture (MPa/m)

s: mass source term (kg/(m^2-s))

T: transmissivity (m^3)

t: time (s)

t_a: Agarwal time (s)

t_D: dimensionless time (unitless)

$t_{D,trans}$: dimensionless transition time (unitless)

t_e: duration of injection (s)

t_{trans}: transition time (s)

V_f: volume of fluid in fracture and wellbore (m^3)

V_{fr}: volume of fluid in fracture (m^3)

V_{wl}: volume of fluid in wellbore (m^3)

Δt: time from start of transient (s)

ΔP: change in pressure since start of transient (MPa)

ΔP_{nw}: wellbore and near wellbore pressure drop (MPa)

$\Delta\sigma_c$: contact stress of a closed fracture (MPa)

$\Delta\sigma_n$: deformation induced change in normal stress (MPa)

μ: fluid viscosity (MPa-s)

ρ: fluid density (kg/m^3)

ρ_0: fluid density at the reference pressure (kg/m^3)

ρ_{fr}: average density of fluid in fracture (kg/m^3)

ρ_{init}: initial fluid density (kg/m^3)

ρ_{inj}: density of injected fluid (kg/m^3)

$\rho_{leakoff}$: average density of fluid leaking off from the fracture (kg/m^3)

ρ_{wl}: average density of fluid in wellbore (kg/m^3)

σ_{hmin}: minimum principal stress (MPa)

σ_n': effective normal stress (MPa)

σ_n: normal stress (MPa)

σ_n^r: remote loading normal stress (MPa)

$\sigma_{n,ref}$: reference normal stress (MPa)

υ: Poisson's ratio (unitless)

ϕ_{init}: initial porosity (unitless)

ϕ: porosity (unitless)

τ: superposition time (unitless)

Metric to oilfield unit conversions

0.305 m/ft

0.159 m^3/bbl

0.454 kg/lbm

0.00689 MPa/psi

9.869×10^{-16} m^2/md

Appendix A: Derivation of the equations governing pressure transient behavior during a DFIT test

In this appendix, we derive the equations governing pressure transient behavior during a DFIT.

We will describe the entire fracture and wellbore system can be described with a "lumped parameter model," in which we assume that $\frac{dP}{dt}$ is uniform throughout the entire system. This approach is isothermal and implicitly neglects pressure gradient due to flow in the well, perforation, near wellbore, and along the fracture. Considering these effects would not fundamentally change the conclusions drawn from the analysis. Related approaches were used by Raaen et al. (2001) and Blasingame and Craig (2006), though the derivation we provide here has important differences.

The pressure derivative with time can be decomposed using the chain rule as:

$$\frac{dP}{dt} = \frac{dP}{dm}\frac{dm}{dt}, \tag{A-1}$$

where m is the total mass of fluid in the wellbore and in the fracture and P is the pressure that is either measured at the bottom of the well or calculated from surface pressure measurements. $\frac{dm}{dt}$ is equal to the surface mass injection rate, $q_{m,inj}$, minus the rate at which fluid mass flows out of the well and fracture into the matrix, $q_{m,leakoff}$. We can expand these terms by saying that:

$$\frac{dm}{dt} = q_{m,inj} - q_{m,leakoff} = q_{inj}\rho_{inj} - q_{leakoff}\rho_{leakoff}, \tag{A-2}$$

where q_{inj} is the volumetric surface injection rate, ρ_{inj} is the density of the fluid injected, $q_{leakoff}$ is the volumetric rate of leakoff into the matrix, and $\rho_{leakoff}$ is the average density of the fluid leaking off into the matrix.

$\frac{dP}{dm}$ can be expanded by starting with the definition:

$$m = \rho_{wl}V_{wl} + \rho_{fr}V_{fr}, \tag{A-3}$$

where ρ_{wl} is the average density of the fluid in the wellbore, V_{wl} is the volume of the wellbore, ρ_{fr} is the average density of the fluid in the fracture, and V_{fr} is the volume of the fracture.

To simplify further, we assume that the fluid is slightly compressible and has constant compressibility, c_f. In this case, we can write:

$$\rho = \rho_0 \exp\left(\left(P - P_0\right)c_f\right), \tag{A-4}$$

where P_0 is a reference pressure and ρ_0 is the density of the fluid at that pressure. Taking the Taylor series expansion and discarding higher order terms provides the approximation:

$$\rho = \rho_0\left(1 + c_f\left(P - P_0\right)\right). \tag{A-5}$$

We can take the derivative of this linearized equation with respect to pressure and determine that:

$$\frac{d\rho}{dP} = \rho_0 c_f. \tag{A-6}$$

Now we take the derivative of Equation A-3 with respect to pressure:

$$\frac{dm}{dP} = \frac{d\rho_{wl}}{dP}V_{wl} + \rho_{wl}\frac{dV_{wl}}{dP} + \frac{d\rho_{fr}}{dP}V_{fr} + \rho_{fr}\frac{dV_{fr}}{dP}. \tag{A-7}$$

Combining Equations A-1, A-2, and A-7, we arrive at:

$$\frac{dP}{dt} = \frac{q_{inj}\rho_{inj} - q_{leakoff}\rho_{leakoff}}{\frac{d\rho_{wl}}{dP}V_{wl} + \rho_{wl}\frac{dV_{wl}}{dP} + \frac{d\rho_{fr}}{dP}V_{fr} + \rho_{fr}\frac{dV_{fr}}{dP}}. \tag{A-8}$$

Equation A-8 can be simplified by relying on the assumption that the fluid is slightly compressible. If we assume that ρ_{inj}, $\rho_{leakoff}$, ρ_{wl}, and ρ_{fr} are all approximately equal (for isothermal fresh water, they would be within a few percent), and these quantities are also equal to the ρ_0 value used to calculate the derivatives of fluid density with respect to pressure in the wellbore and the fracture, then we can cancel them out of the numerator and the denominator of Equation A-8 and arrive at:

$$\frac{dP}{dt} = \frac{q_{inj} - q_{leakoff}}{c_f V_{wl} + \frac{dV_{wl}}{dP} + c_f V_{fr} + \frac{dV_{fr}}{dP}} = \frac{q_{inj} - q_{leakoff}}{C_t}, \tag{A-9}$$

where C_t is the total storage coefficient of the entire system. The definition of total storage coefficient used in Equation A-9 is more general than the expression used by Raaen et al. (2001) or by Craig and Blasingame (2006).

Craig and Blasingame (2006) defined the after closure storage coefficient as (using slightly different variable definitions):

$$C_{ac} = c_f V_w + c_f V_{fr}, \tag{A-10}$$

where V_{fr} is assumed constant. Comparing this expression to Equation A-9, we can see that Craig and Blasingame (2006), without stating this assumption, have assumed that $\rho_{wl}\frac{dV_{wl}}{dP}$ and $\rho_{fr}\frac{dV_{fr}}{dP}$ are zero. The former term, the changing wellbore volume, is routinely assumed negligible. However, the latter term, for the changing fracture volume after closure, is large, as shown below. Craig and Blasingame (2006) permitted that the fluid in the wellbore and fracture may have different compressibility, while we assumed that their compressibility is the same. The distinction should have a negligible effect in a DFIT, where clear water is injected.

Raaen et al. (2001) used an approach similar to shown in Equation A-9. However, they assumed that "when the fracture is closed, there are three main contributions to the system stiffness: from the compliance of the wellbore fluid, from the deformation of the casing and top-side tubes, and from the deformation of the openhole below the casing shoe." Therefore, without stating this assumption, they are assuming that the $\frac{d\rho_{fr}}{dP}\ V_{fr}$ and $\rho_{fr}\frac{dV_{fr}}{dP}$ terms in Equation A-9 are zero.

Under the assumptions we have described, Equation A-9 applies during all phases of a fracturing test: during injection, the before-closure shut-in period, during closure, and the after-closure shut-in period. In reality, during injection, pressure gradient due to flow through the well, perforations, near wellbore region, and fracture would cause $\frac{dP}{dt}$ to vary spatially throughout the system, but after the early shut-in period, these pressure gradients should be minimal.

The total storage coefficient has four parts: compressibility of fluid in the wellbore, changes in the wellbore volume, compressibility of the fluid in the fracture, and changes in fracture volume. Conventionally, changes in wellbore volume are assumed negligible relative to $c_f V_{wl}$ and the $\frac{dV_{wl}}{dP}$ term is neglected (Horne, 1995).

$\frac{dV_{fr}}{dP}$ can be written as $\frac{A}{S_f}$, where A is the surface area of the fracture and S_f is the fracture stiffness, the derivative of effective normal stress with respect to aperture (Jaeger et al., 2007). $\frac{dV_{fr}}{dP}$ depends on fracture geometry and mechanical characteristics of the formation. In practice, the fracture geometry is usually not well-constrained. Two limiting cases for fracture geometry are circular and PKN (for the Perkins-Kern-Nordgren model; Perkins and Kern, 1961; Nordgren, 1972). If there is no fracture height restraint due to layering, then the fracture will be approximately circular (though not completely circular because the trends in stress with depth will cause it to preferentially propagate upward). If the fracture is confined between higher stress intervals, then the fracture length will be much greater than its height, and stiffness can be approximated from a 2D plane strain solution, the key assumption of the PKN model.

For a radial fracture, the stiffness of the fracture (when open), $S_{f,o}$, can be written as (Sneddon, 1946):

$$S_{f,r} = \frac{3\pi G_m}{8(1-\nu)R_f}, \tag{A-11}$$

where G_m is the shear modulus, υ is Poisson's ratio, and R_f is the radius. For a fracture with length much longer than its height, the stiffness can be estimated as (Sneddon, 1946; Perkens and Kern, 1961; Nordgren 1972):

$$S_{f,PKN} = \frac{4G_m}{\pi(1-\nu)h_f}. \tag{A-12}$$

The magnitudes of the $\frac{A}{S_f}$, $c_f V_{wl}$, and $c_f\, V_{fr}$ terms can be roughly assessed. For example, in the fracture simulation shown in Section 3.1.2. The final fracture length is about 250 m, with a height of 7 m, for a surface area of 1750 m^2. Figure 7 shows that the average fracture aperture is roughly 1 mm, which means that V_{fr} is equal to roughly 1.75 m^3 and $c_f V_{fr}$ is equal to roughly (using the value of water compressibility given in Table 1) to 0.0008 m^3/MPa. V_{wl} depends on wellbore length and diameter. A typical value is around 100 m^3, and so $c_f V_{fr}$ can be estimated as 0.0458 m^3/MPa. The fracture shown in Figure 7 has length much greater than height, 7 m. Therefore, its preclosure stiffness can be assessed from Equation A-12 and is equal to 3.638 MPa/mm. The $\frac{A}{S_f}$ term is equal to 0.48 m^3/MPa. This analysis indicates that the dominant effect in the total storage coefficient is likely to be the fracture stiffness, the wellbore storage has minor but nonnegligible effect, and the compressibility of the water in the fracture is negligible.

After shut-in, the pressure derivative can be written as (assuming constant wellbore volume and that the $c_f\, V_{fr}$ term is negligible):

$$\frac{dP}{dt} = \frac{-q_{leakoff}}{c_f V_{wl} + \frac{A}{S_f}}. \tag{A-13}$$

If the fracture continues propagating after closure, A may change significantly and S_f may change (depending on the geometry). If the fracture is no longer propagating, S_f will be constant prior to fracture closure, but will change when the fracture closes.

Using the Carter model to calculate leakoff rate yields a value of $q_{leakoff}$ that scales with the inverse of the square root of time (Howard and Fast, 1957). This is why plots of pressure versus the square root of time during shut-in yield a straight line. If leakoff rate scales with time according to the G-function introduced by Nolte (1979), then a plot of pressure versus G-time will yield a straight line. The straight line will only occur if the denominator in Equation A-13 is constant, which is why closure causes a deviation from the straight line. Closure also decreases the fracture transmissivity. If this causes the fracture to no longer be "infinite conductivity," then pressure gradients can develop along the fracture, and this can cause the "lumped parameter" approach used in this section to no longer be applicable.

To understand the pressure trend after closure, it is necessary to investigate how stiffness is affected by closure. The stiffness after closure, $S_{f,c}$, includes the effect of the elastic response of the formation (as shown in Equations A-11 and A-12), but also includes a contribution from the contacting fracture walls (Section 12.3 from Jaeger et al., 2007).

As a simplifying assumption, we assume that both the stress and aperture are constant along the fracture. This is not strictly correct, but is sufficiently accurate for providing a conceptual explanation. Under this simplifying assumption, we can write:

$$\sigma_n^{'} = \sigma_n^{r} + ES_{f,o} - P. \qquad \text{(A-14)}$$

Because the initial aperture of a hydraulic fracture is zero (since it does not initially exist), backstress is created by its entire aperture, E.

To find the fracture stiffness, Equation A-14 can be solved for P and differentiated with respect to E:

$$S_{f,c} = \left(\frac{dE}{dP}\right)^{-1} = \frac{dP}{dE} = S_{f,o} - \frac{d\sigma'}{dE} = S_{f,o} - \left(\frac{dE}{d\sigma_{n'}}\right)^{-1} = S_{f,o} + \left(\frac{dE}{dP}\right)^{-1} = S_{f,o} + S_{f,cont}, \qquad \text{(A-15)}$$

where $S_{f,cont}$ is the contribution to the stiffness from the contact stress. $S_{f,cont}$ can be calculated from any constitutive equation the specifies E as a function of effective normal stress. For example, Equation 12 yields:

$$S_{f,cont} = -\left(\frac{dE}{d\sigma_n'}\right)^{-1} = \left(\frac{9E_0}{\sigma_{n,ref}}\left(1 + \frac{9\sigma_n'}{\sigma_{n,ref}}\right)^{-2}\right)^{-1} = \frac{\sigma_{n,ref}}{9}\frac{E_0}{E^2}. \qquad \text{(A-16)}$$

Thus, using Equation 12, the stiffness of a closed fracture is:

$$S_{f,c} = S_{f,o} + \frac{\sigma_{n,ref}}{9}\frac{E_0}{E^2} \qquad \text{(A-17)}$$

The value of $S_{f,cont}$ increases as the fracture closes. At closure:

$$S_{f,cont}^{closure} = \frac{\sigma_{n,ref}}{9E_0}. \qquad \text{(A-18)}$$

Referring back to the simulation described in Section 3.1.2, we can calculate $S_{f,cont}^{closure}$ to be 11.333 MPa/mm (for a total S_f of 14.971 MPa/mm), significantly greater than the value of $S_{f,o}$, 3.638 MPa/mm. Closure causes a sharp increase in S_f from $S_{f,o}$ to $S_{f,c}$, which (from Equation A-13), causes an increase in the pressure derivative. The derivative increases very sharply because stiffness increases so much with closure, increasing by roughly a factor of four, and continuing to increase further as aperture drops further below E_0. In Section 3.1.3, a simulation is shown with a smaller value of $\sigma_{n,ref}$, 5 MPa instead of 51 MPa, and so $S_{f,cont}^{closure}$ is 1.111 MPa/mm (for a total S_f of 4.749 MPa/mm), causing only a modest increase compared to the stiffness prior to closure. As a result, the derivative increases less abruptly.

Appendix B: Derivation of expression for time until transition from early linear to late linear flow

In this section, we consider the pressure transient that results from linear (1D) leakoff of a fixed volume of fluid from an infinite conductivity fracture. The pressure transient after a DFIT can be idealized as a slug test, an instantaneous injection of fluid into the wellbore and fracture, followed by leakoff of that fluid into the matrix (Ramey and Agarwal, 1972; Ayoub et al., 1988; Peres et al., 1993; Craig and Blasingame, 2006).

For simplicity, we neglect the effect of closure and assume that the fracture compliance, $C_f = \frac{1}{S_f} = \frac{dE}{dP}$, is constant. The fracture is assumed to be effectively infinite conductivity (valid for C_{fD} greater than 300), so it can be treated as having a single, uniform pressure. With wellbore storage, the total storage coefficient of the system, C_t, equals $C_f \times A + C_w$, where C_w is the wellbore storage coefficient.

At early time, the difference between the fluid pressure in the fracture and the initial reservoir pressure is nearly constant with respect to time. If we assume that leakoff from the fracture is linear, we can use the Carter leakoff model (Howard and Fast, 1957). Accounting for leakoff from both sides of the fracture, the cumulative leakoff is:

$$Q_{cum} = 4A\sqrt{t}\ (P_{f,init} - P_{init})\sqrt{\frac{\phi c_t k}{\pi \mu}}, \tag{B-1}$$

where $P_{f,init}$ is the initial fluid pressure inside the fracture, Q_{cum} is the cumulative leakoff, A is the fracture surface area, and P_{init} is the initial reservoir fluid pressure.

Because we have made the assumption fracture compliance remains constant, the total amount of fluid stored in the crack and the wellbore (relative to the amount stored when the fluid pressure equals P_{init}) is defined as S and equal to:

$$S = \left(A\frac{dE}{dP} + C_w \right)\left(P_{f,init} - P_{init} \right) = AC_t \left(P_{f,init} - P_{init} \right), \tag{B-2}$$

where, in analogy to Equation A-9:

$$C_t = C_w + \frac{C_f}{A}. \tag{B-3}$$

Using these expressions, we can write the mass balance equation for the system:

$$C_t A(P - P_{init}) = C_t A(P_{f,init} - P_{init}) - 4A\sqrt{\frac{kc_t\phi}{\pi\mu}}(P_{f,init} - P_{init})\sqrt{t}\,. \tag{B-4}$$

If we define dimensionless time as:

$$t_D = 16\left(\frac{1}{C_t}\right)^2 \frac{kc_t\phi}{\pi\mu}t\,, \tag{B-5}$$

and we define dimensionless pressure as:

$$P_D = \frac{P - P_{init}}{P_{f,init} - P_{init}}, \tag{B-6}$$

then we can write the mass balance equation as a simple expression giving the evolution of pressure with respect to time:

$$P_{DE} = 1 - \sqrt{t_D}\,. \tag{B-7}$$

Equation B-7 is only applicable at early time, because the leakoff rate is calculated assuming constant pressure in the fracture, and for one-dimensional leakoff.

At late time, the pressure transient will be found by taking the derivative of the solution for constant rate injection (Houze et al., 1988; Ayoub et al., 1988; Gu et al., 1993). The solution for constant rate injection into an infinite conductivity fracture, neglecting the fluid storage of the wellbore, is (Gringarten et al., 1974):

$$P = P_{init} - \frac{Q}{A}\sqrt{\frac{\mu}{\pi k}\frac{1}{c_t\phi}}\sqrt{t}\,, \tag{B-8}$$

where Q is the volumetric injection rate. Taking the derivative, we find the solution for injection of a volume of fluid Q_{slug} into the system:

$$P = P_{init} - \frac{Q_{slug}}{2A}\sqrt{\frac{\mu}{\pi k}\frac{1}{c_t\phi}}\frac{1}{\sqrt{t}}. \tag{B-9}$$

For our problem,

$$Q_{slug} = AC_t(P_{f,init} - P_{init}). \tag{B-10}$$

So we can write:

$$P = P_{init} - \frac{1}{2}C_t(P_{f,init} - P_{init})\sqrt{\frac{\mu}{\pi k}\frac{1}{c_t\phi}}\frac{1}{\sqrt{t}}. \tag{B-11}$$

Using the same dimensionless variables as before, we can write:

$$P_{DL} = \frac{2}{\pi}\frac{1}{\sqrt{t_D}}. \tag{B-12}$$

So now we have expressions for dimensionless pressure as a function of dimensionless time for the early part of the transient and the late part of the transient. There is not a simple expression to describe evolution of pressure during the transition between these two limiting cases. However, we can produce a simple estimate for the time at which the transition occurs.

We enforce that:

$$\left(\frac{dP_{DE}}{dt_D}\right) = \left(\frac{dP_{DL}}{dt_D}\right) \text{for } t_D = t_{D,trans}. \tag{B-13}$$

Solving this equation we find that:

$$t_{D,trans} = \frac{2}{\pi}, \tag{B-14}$$

which in dimensional form is:

$$t_{trans} = \frac{1}{8} C_t^2 \frac{\mu}{k c_t \phi}. \tag{B-15}$$

To confirm this expression, a simple numerical model was set up and run. The model simulated the solution to the classical diffusivity equation in 1D in an infinite half-space using the finite difference method with logarithmically spaced elements, implicit timestepping, and adaptive timestepping. The simulation also included fluid storage at the boundary of the model with constant storage coefficient (to represent the fluid stored in the fracture and wellbore). Figure 23 below compares the approximate analytical solutions and the numerical solution.

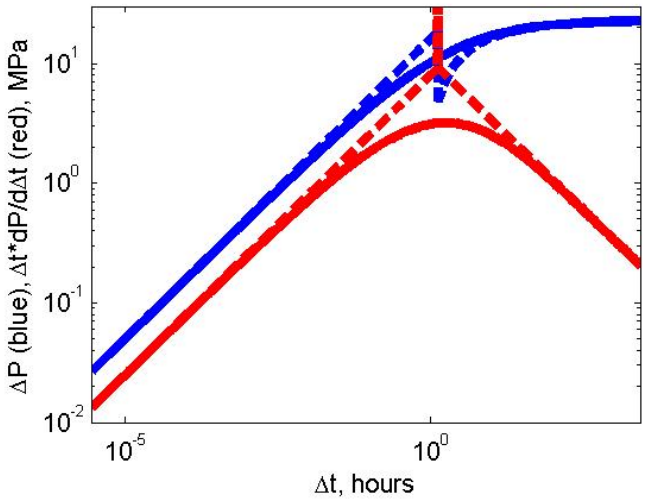

Figure 23: Bourdet plot with derivative with respect to time for a slug test with 1D leakoff and wellbore storage. Comparison of simulation results (solid lines) and approximate analytical expressions (dashed lines).

At early and late time, the approximate solutions are very close to the fully numerical solution. During the period of transition, they deviate strongly. The figure confirms that the point in time at which the derivatives of the analytical expressions are equal is a good approximation to the point in time when the transition occurs between the two limiting cases.

References

Agarwal, Ram G. 1980. A new method to account for producing time effects when drawdown type curves are used to analyze pressure buildup and other test data. Paper SPE 9289 presented at the SPE Annual Technical Conference and Exhibition, Dallas, TX, doi: 10.2118/9289-MS.

Ayoub, J. A., D. P. Bourdet, Y. L. Chauvel. 1988. Impulse testing. *SPE Formation Evaluation* **3** (3): 534-546, doi: 10.2118/15911-PA.

Babazadeh, Mohsen, Mark McClure. 2015. Coupling fluid flow and geomechanics in a three-dimensional discrete fracture network simulator. Paper presented at the 49th US Rock Mechanics / Geomechanics Symposium, San Francisco, CA.

Barree, R. D. 1983. A practical numerical simulator for three-dimensional fracture propagation in heterogeneous media. Paper SPE 12273 presented at the SPE Reservoir Simulation Symposium, San Fransisco, CA.

Barree, R. D. 1998. Applications of pre-frac injection/falloff tests in fissured reservoirs - field examples. Paper SPE 39932 presented at the SPE Rocky Mountain Regional/Low Permeability Reservoirs Symposium, Denver, CO, doi: 10.2118/39932-MS.

Barree, R. D., V. L. Barree, D. P. Craig. 2007. Holistic fracture diagnostics. Paper SPE 107877 presented at the SPE Rocky Mountain Oil & Gas Technology Symposium, Denver, CO, doi: 10.2118/107877-MS.

Barree, R. D., H. Mukherjee. 1996. Determination of pressure dependent leakoff and its effect on fracture geometry. Paper SPE 36424 presented at the 71st Annual Technical Conference and Exhibition, Denver, CO, doi: 10.2118/36424-MS.

Barree, R. D., J. L. Miskimins, J. V. Gilbert. 2014. Diagnostic fracture injection tests: common mistakes, misfures, and misdiagnoses. *SPE Production & Operations* **30** (2), doi: 10.2118/169539-PA.

Barton, N., S. Bandis, K. Bakhtar. 1985. Strength, deformation and conductivity coupling of rock joints. International Journal of Rock Mechanics and Mining Sciences & Geomechanics Abstracts 22 (3): 121-140, doi: 10.1016/0148-9062(85)93227-9.

Blasingame, T. A., W. J. Lee. 1986. Variable-rate reservoir limits testing. Paper SPE 15028 presented at the Permian Basin Oil and Gas Recovery Conference, Midland, TX, doi: 10.2118/15028-MS.

Bourdet, Dominique, J. A. Ayoub, Y. M. Pirard. 1989. Use of pressure derivative in well-test interpretation. SPE Formation Evaluation 4 (2): 293-302, doi: 10.2118/12777-PA.

Branagan, P. T., N. R. Warpinski, B. Engler, R. Wilmer. 1996a. Measuring the hydraulic fracture-induced deformation of reservoir and adjacent rocks employing a deeply buried inclinometer array: GRI/DOE Multi-Site Project. Paper SPE 36451 presented at the SPE Annual Technical Conference and Exhibition, Denver, CO, doi: 10.2118/36451-MS.

Branagan, P. T., R. E. Peterson, N. R. Warpinski, T. B. Wright. 1996b. Characterization of a remotely intersected set of hydraulic fractures: results of Intersection Well No. 1-B, GRI/DOE Multi-Site Project. Paper SPE 36452 presented at the SPE Annual Technical Conference and Exhibition, Denver, CO, doi: 10.2118/36452-MS.

Brown, Stephen R., Ronald L. Bruhn. 1998. Fluid permeability of deformable fracture networks. *Journal of Geophysical Research* **103** (B2): 2489-2500.

Castillo, J.L. 1987. Modified fracture pressure decline analysis including pressure-dependent leakoff. Paper SPE 164417 presented at the SPE/DOE Low Permeability Reservoir Symposium, Denver, CO, doi: 10.2118/16417-MS.

Craig, David P. 2014. New type curve analysis removes limitations of conventional after-closure analysis of DFIT data. Paper SPE 168988-MS presented at the SPE Unconventional Resources Conference - USA, The Woodlands, TX, doi: 10.2118/168988-MS.

Craig, D. P., T. A. Blasingame. 2006. Application of a new fracture-injection/falloff model accounting for propagating, dilated, and closing hydraulic fractures. Paper SPE 100578 presented at the SPE Gas Technology Symposium, Calgary, Alberta, Canada, doi: 10.2118/100578-MS.

Cramer, D. D. 1987. The application of limited-entry techniques in massive hydraulic fracturing treatments. Paper SPE 16189 presented at the SPE Production Operations Symposium, Oklahoma City, OK, doi: 10.2118/16189-MS.

Cramer, D. D., D. H. Nguyen. 2013. Diagnostic fracture injection testing tactics in unconventional reservoirs. Paper SPE 163863 presented at the SPE Hydraulic Fracturing Technology Conference, Woodlands, TX, doi: 10.2118/163863-MS.

Crouch, Steven L., A. M. Starfield. 1983. Boundary Element Methods in Solid Mechanics: with Applications in Rock Mechanics and Geological Engineering. London; Boston, Allen & Unwin.

Economides, Michael J., Kenneth G. Nolte. 2000. Reservoir Stimulation, 3rd edition. Chichester, England; New York, John Wiley.

Gangi, Anthony F. 1978. Variation of whole and fractured porous rock permeability with confining pressure. International Journal of Rock Mechanics and Mining Sciences 15: 249-257, doi: 10.1016/0148-9062(78)90957-9.

Geertsma, J., F. de Klerk. 1969. A rapid method of predicting width and extent of hydraulically induced fractures. Journal of Petroleum Technology 21 (12): 1571-1581, doi: 10.2118/2458-PA.

Godbey, J. K., H. D. Hodges. 1958. Pressure measurements during formation fracturing operations. Petroleum Transactions, AIME 213: 65-69.

Gringarten, Alain C., Henry J. Ramey, R. Raghavan. 1974. Unsteady-state pressure distributions created by a well with a single infinite conductivity vertical fracture. SPE Journal 14 (4): 347-360, doi: 10.2118/4051-PA.

Gu, H., J. L. Elbel, K. G. Nolte, A. H. D. Cheng, Y. Abousleiman. 1993. Formation permeability determination using impulse-fracture injection. Paper SPE 25425 presented at the Production Operations Symposium, Oklahoma City, OK, doi: 10.2118/25425-MS.

Haimson, Bezalel, Charles Fairhurst. 1967. Initiation and extension of hydraulic fractures in rocks. Society of Petroleum Engineers Journal 7 (3), doi: 10.2118/1710-PA.

Horne, Roland N. 1995. *Modern Well Test Analysis: a Computer-Aided Approach*, 2nd edition. Palo Alto, CA, Petroway, Inc.

Houze, Olivier P., Roland N. Horne, Henry J. Ramey. 1988. Pressure-transient response of an infinite conductivity vertical fracture in a reservoir with double-porosity behavior. SPE Formation Evaluation 3 (3): 510-518, doi: 10.2118/12778-PA.

Howard, G., C.R. Fast. 1957. Optimum fluid characteristics for fracture extension. Drilling and Production Practice 24: 261-270.

Hubbert, M. K., D. G. Willis. 1957. Mechanics of hydraulic fracturing. Journal of Petroleum Technology 9 (6): 153-168.

Jeffrey, R. G. 1989. The combined effect of fluid lag and fracture toughness on hydraulic fracture propagation. Paper SPE 18957 presented at the Low Permeability Reservoirs Symposium, Denver, CO, doi: 10.2118/18957-MS.

Khristianovich, S. A., Y. P. Zheltov. 1959. Theoretical principles of hydraulic fracturing of oil strata. Paper presented at the Fifth World Petroleum Congress, New York, New York.

Koning, E. J. L., H. Niko. 1985. Fractured water-injection wells: a pressure falloff test for determining fracture dimensions. Paper SPE 14458 presented at the SPE Annual Technical Conference and Exhibition, Las Vegas, Nevada, doi: 10.2118/14458-MS.

Mack, Mark G., Norman Warpinski, R. 2000. Mechanics of Hydraulic Fracturing. In *Reservoir Stimulation*, ed. Michael J. Economides and Kenneth G. Nolte. Wiley.

Mahrer, Kenneth D. 1999. A review and perspective on far-field hydraulic fracture geometry studies. Journal of Petroleum Science and Engineering 24 (1): 13-28, doi: 10.1016/S0920-4105(99)00020-0.

Marongiu-Porcu, M., C. A. Ehlig-Economides, M. J. Economides. 2011. Global model for fracture falloff analysis. Paper SPE 144028 presented at the SPE North American Unconventional Gas Conference and Exhibition, The Woodlands, TX, doi: 10.2118/144028-MS.

Marongiu-Porcu, Matteo, Albertus Retnanto, Michael J. Economides, Christine Ehlig-Economides. 2014. Comprehensive fracture calibration test design. Paper SPE 168634 presented at the SPE Hydraulic Fracturing Technology Conference, The Woodlands, TX, doi: 10.2118/168634-MS.

McClure, Mark W. 2014a. Diagnostic fracture injection tests with complex fracture networks. The Leading Edge 33 (5): 546-548, 550-552, doi: 10.1190/tle33050546.1.

McClure, Mark W. 2014b. The potential effect of network complexity on recovery of injected fluid following hydraulic fracturing. Paper SPE 168991 presented at the SPE Unconventional Resources Conference - USA, The Woodlands, TX, doi: 10.2118/168991-MS.

McClure, Mark W., Mohsen Babazadeh, Sogo Shiozawa, and Jian Huang. 2015. Fully coupled hydromechanical simulation of hydraulic fracturing in three-dimensional discrete fracture networks. Paper SPE 170956 presented at the SPE Hydraulic Fracturing Technology Conference, The Woodlands, TX.

McClure, Mark W., Christopher A. J. Blyton, Hojung Jung, and Mukul M. Sharma. 2014. The effect of changing fracture compliance on pressure transient behavior during diagnostic fracture

injection tests. Paper SPE 170956 presented at the SPE Annual Technical Conference and Exhibition, Amsterdam, The Netherlands.

McClure, M. W., R. N. Horne. 2010. Discrete fracture modeling of hydraulic stimulation in Enhanced Geothermal Systems. Paper presented at the Thirty-Fifth Workshop on Geothermal Reservoir Engineering, Stanford University.

McClure, Mark W., Roland N. Horne. 2013. Discrete Fracture Network Modeling of Hydraulic Stimulation: Coupling Flow and Geomechanics: SpringerBriefs in EarthSciences, Springer.

Meng, Chunfang, Lingli Wei, Roger Yuan. 2014. Coupled fluid flow and geomechanics modeling for DFIT analysis in unconventional gas development. Paper presented at the International Petroleum Technology Conference, Kuala Lumpur, Malaysia, doi: 10.2523/18159-MS.

Mohamed, I. M., R. A. Nasralla, M. A. Sayed, M. Marongiu-Porcu, C. A. Ehlig-Economides. 2011. Evaluation of after-closure analysis techniques for tight and shale gas formations. Paper SPE 140136 presented at the SPE Hydraulic Fracturing Technology Conference, The Woodlands, TX, doi: 10.2118/140136-MS.

Moody, Lewis F. 1944. Friction factors for pipe flow. *Transactions of the A.S.M.E* **66** (8): 671-684.Nolte, Kenneth. 1979. Determination of fracture parameters from fracturing pressure decline. Paper SPE 8341 presented at the SPE Annual Technical Conference and Exhibition, Las Vegas, Nevada.

Nolte, Kenneth G. 1991. Fracturing-pressure analysis for nonideal behavior. Journal of Petroleum Technology 43 (2): 210-218, doi: 10.2118/20704-PA.

Nolte, K. G., M. G. Mack, W. L. Lie. 1993. A systematic method for applying fracturing pressure decline: Part I. Paper SPE 25845 presented at the SPE Rocky Mountain Regional/Low Permeability Reservoirs Symposium, Denver, CO, doi: 10.2118/25845-MS.

Nolte, Kenneth G., Michael B. Smith. 1981. Interpretation of fracturing pressures. Journal of Petroleum Technology 33 (9): 1767-1775, doi: 10.2118/8297-PA.

Nordgren, R. P. 1972. Propagation of a vertical hydraulic fracture. Society of Petroleum Engineers Journal 12 (4): 306-314, doi: 10.2118/3009-PA.

Nowacki, W. 1986. *Thermoelasticity*, Pergamon Press.

Okada, Yoshimitsu. 1992. Internal deformations due to shear and tensile faults in a half-space. Bulletin of the Seismological Society of America 82 (2): 1018-1040.

Olson, J. E. 2007. Fracture aperture, length and pattern geometry development under biaxial loading: a numerical study with applications to natural, cross-jointed systems. In The Relationship between Damage and Localization, ed. H. Lewis and G. D. Couples, 123-142. Geological Society, London, Special Publications, The Geological Society of London.

Padmakar, A.S. 2013. Geomechanics coupled reservoir flow simulation for diagnostic fracture injection test design and interpretation in shale reservoirs. Paper 166201 presented at the SPE Annual Technical Conference and Exhibition, New Orleans, LA, doi: 10.2118/166201-MS.

Peres, Alvaro, Mustafa Onur, Albert Reynolds. 1993. A new general pressure-analysis procedure for slug tests. SPE Formation Evaluation 8 (4): 292-298, doi: 10.2118/18801-PA.

Perkins, T. K., L. R. Kern. 1961. Widths of hydraulic fractures. Journal of Petroleum Technology 13 (9): 937-949, doi: 10.2118/89-PA.

Perkins, T. K., J. A. Gonzalez. 1985. The effect of thermoelastic stresses on injection well fracturing. *SPE Journal* **25** (1): 78-88, doi: 10.2118/11332-PA.

Plahn, S.V., K. G. Nolte, L.G. Thompson, S. Miska. 1997. A quantitative investigation of the fracture pump-in/flowback test. *SPE Production & Facilities* **12** (1): 20-27, doi: 10.2118/30504-PA.

Pyrak-Nolte, L.J., J. P. Morris. 2000. Single fractures under normal stress: the relation between fracture specific stiffness and fluid flow. International Journal of Rock Mechanics and Mining Sciences 37: 245-262, doi: 10.1016/S1365-1609(99)00104-5.

Raaen, A. M., M. Brudy. 2001. Pump-in/flowback tests reduce the estimate of horizontal in-situ stress significantly. Paper SPE 71367 presented at the SPE Annual Technical Conference and Exhibition, New Orleans, LA, doi: 10.2118/71367-MS.

Raaen, A. M., E. Skomedal, H. Kjorholt, P. Markestad, D. Okland. 2001. Stress determination from hydrualic fracturing tests: the system stiffness approach. *International Journal for Rock Mechanics and Mining Sciences* **38** (4): 529-541, doi: 10.1016/S1365-1609(01)00020-X.

Ramey, Henry J., Ram G. Agarwal. 1972. Annulus unloading rates as influenced by wellbore storage and skin effect. SPE Journal 12 (5): 453-462, doi: 10.2118/3538-PA.

Ribeiro, Priscilla, Roland Horne. 2013. Pressure and temperature transient analysis: hydraulic fractured well application. Paper SPE 166222 presented at the SPE Annual Technical Conference and Exhibition, New Orleans, LA, doi: 10.2118/166222-MS.

Shlyapobersky, J. W., W. W. Walhaug, R. E. Sheffield, P. T. Huckabee. 1988. Field determination of fracturing parameters, for overpressure calibrated design of hydraulic fracturing. Paper SPE 18195 presented at the SPE Annual Technical Conference and Exhibition, Houston, TX, doi: 10.2118/18195-MS.

Sneddon, I. N. 1946. The distribution of stress in the neighborhood of a crack in an elastic solid. Proceedings of the Royal Society of London Series A 187 (1009): 229-260, doi: 10.1098/rspa.1946.0077.

Soliman, M. Y., A. A. Daneshy. 1991. Determination of fracture volume and closure pressure from pump-in/flowback tests. Paper SPE 21400 presented at the SPE Middle East Oil Show, Bahrain, doi: 10.2118/21400-MS.

Soliman, M. Y., Talal Gamadi. 2012. Testing tight gas and unconventional formations and determination of closure pressure. Paper SPE 150948 presented at the SPE/EAGE European Unconventional Resources Conference and Exhibition, Vienna, Austria, doi: 10.2118/150948-MS.

Soliman, M. Y., C.S. Kabir. 2012. Testing unconventional formations. Journal of Petroleum Science and Technology 92-93: 102-109, doi: 10.1016/j.petrol.2012.04.027.

Valko, P. P., M. J. Economides. 1999. Fluid-leakoff delineation in high-permeability fracturing. SPE Production & Facilities 14 (2): 117-130, doi: 10.2118/56135-PA.

van den Hoek, P. J. 2002. Pressure transient analysis in fractured produced water injection wells. Paper SPE 77946 presented at the SPE Asia Pacific Oil and Gas Conference and Exhibition, Melbourne, Australia, doi: 10.2118/77946-MS.

Vinsome, P. K., J. Westerveld. 1980. A simple method for predicting cap and base rock heat loses in thermal reservoir simulators. Journal of Canadian Petroleum Technology 19 (3): 87-90, doi: 10.2118/80-03-04.

Wallace, J., C.S. Kabir, C. L. Cipolla. 2014. Multiphysics investigation of diagnostic fracture injection tests in unconventional reservoirs. Paper 168620 presented at the SPE Hydraulic Fracturing Technology Conference, The Woodlands, TX, doi: 10.2118/168620-MS.

Walsh, J. B. 1981. Effect of pore pressure and confining pressure on fracture permeability. International Journal of Rock Mechanics and Mining Sciences 18: 429-435, doi: 10.1016/0148-9062(81)90006-1.

Warpinski, N. R., J. C. Lorenz, P. T. Branagan, F. R. Myal, B. L. Gall. 1993. Examination of a cored hydraulic fracture in a deep gas well, SPE 22876. *SPE Production & Facilities* **8** (3): 150-158, doi: 10.2118/22876-PA.

Warpinski, N. R., L. W. Teufel. 1987. Influence of geologic discontinuities on hydraulic fracture propagation. Journal of Petroleum Technology 39 (2): 209-220, doi: 10.2118/13224-PA.

Willis-Richards, J., K. Watanabe, H. Takahashi. 1996. Progress toward a stochastic rock mechanics model of engineered geothermal systems. Journal of Geophysical Research 101 (B8): 17481-17496, doi: 10.1029/96JB00882.

Witherspoon, P. A., J. S. Y. Wang, K. Iwai, J. E. Gale. 1980. Validity of cubic law for fluid flow in a deformable rock fracture. *Water Resources Research* **16** (6): 1016-1024, doi: 10.1029/WR016i006p01016.

Yew, C. H., G. H. Liu. 1993. The fracture tip and critical stress intensity factor of a hydraulically induced fracture. *SPE Production & Facilities* **8** (3): 171-177, doi: 10.2118/22875-PA.

Zhang, Junjing, Anton Kamenov, D. Zhu, A.D. Hill. 2013. Laboratory measurement of hydraulic fracture conductivities in the Barnett Shale Paper SPE 163839 presented at the SPE Hydraulic Fracturing Technology Conference, The Woodlands, TX, doi: 10.2118/163839-MS.

Zoback, Mark D. 2007. Reservoir Geomechanics. Cambridge, Cambridge University Press.